nature cardiovascular research

Article

https://doi.org/10.1038/s44161-025-00659-5

Reversal of cerebrovascular anomalies in a zebrafish model of vein of Galen aneurysm

Received: 12 July 2023

Accepted: 24 April 2025

Published online: 12 June 2025

Check for updates

Edwige Martin-Valiente[1,2,8], Yao Du[1,8], Chloé Goemans[1], Michelle America[2], Egor Zindy[3], Myckel Adam[2], Benoit Scheid[4], Miikka Vikkula[5,6], Boris Lubicz[7], Benoit Vanhollebeke[2,6] & Nicolas Baeyens[1]

Congenital vascular malformations result from abnormal development of the vascular tree, with the aneurysmal malformation of the vein of Galen (VGAM) being the most prevalent neurovascular malformation in neonates, associated with poor outcomes. This condition is linked to germline mutations in the *RASA1* and *EPHB4* genes, although the underlying developmental mechanisms remain unclear. Here we generate zebrafish models lacking *rasa1a* and *ephb4a* that replicate the genetic and structural features of VGAMs. Our findings connect the development of malformations to insufficient fusion of precursor blood vessels, a process regulated by blood flow and the responses of endothelial cells. RASA1 deficiency destabilizes the homeostatic response to blood flow and contributes to impaired flow-mediated activation of MAPK and phosphatidylinositol-3-kinase signaling. By pharmacologically targeting these signaling pathways in mutant models, we restore normal fusion in existing malformations, offering potential new strategies for treating VGAMs and similar vascular remodeling disorders.

The formation of the vascular network involves a finely regulated chain of events, from generating polarized tubular structures forming a lumen to blood vessel specification. This network further consolidates in a mature tree, with arterioles pouring blood into the capillary network, then collecting back in venules and veins, providing optimal perfusion of the organs. The maturation process requires remodeling by pruning[1], intussusception[2] or fusion[3] of immature vessels during development. These remodeling events happen in perfused vessels and are directly controlled by endothelial cells' perception of flowing blood, with mechanotransduction acting as a critical regulator in the maturation of the vascular network[4]. Congenital vascular anomalies are morphogenetic defects of the vascular system, in which the vascular tree's hierarchization and the vessels' architecture are locally affected.

Congenital vascular anomalies, especially high-flow arteriovenous malformations (AVMs), can develop during the flow-dependent maturation of the vascular tree. High-flow AVMs associated with loss-of-function mutations of bone morphogenic (BMP) signaling, as seen in hereditary hemorrhagic telangiectasia (HHT), are consecutive to disturbed vessel homeostasis. Disturbed endothelial cell quiescence mediated by fluid forces generated by blood flow leads to arteriovenous shunts in high-shear-stress areas[5]. Sensing and integrating physiological values of laminar blood flow are associated with anti-inflammatory and stabilization programs essential for vessel homeostasis. BMP signaling is associated with a physiological shear stress set point[6], underlining its importance in flow-associated vessel quiescence. An inadequate balance in flow-mediated BMP signaling leads to endothelial cell proliferation and migration, improper recruitment of mural cells and the

[1]Laboratoire de Physiologie et Pharmacologie, Faculté de Médecine, Université libre de Bruxelles, Brussels, Belgium. [2]Laboratory of Neurovascular Signaling, Department of Molecular Biology, ULB Neuroscience Institute, Université libre de Bruxelles, Gosselies, Belgium. [3]DIAPath, Center for Microscopy and Molecular Imaging (CMMI), ULB, Gosselies, Belgium. [4]Transfer, Interfaces and Processes (TIPs), Brussels Engineering School, Université libre de Bruxelles, Brussels, Belgium. [5]Human Molecular Genetics, de Duve Institute, UCLouvain, Brussels, Belgium. [6]WEL Research Institute, Wavre, Belgium. [7]Department of Interventional Neuroradiology, Erasme Hospital, HUB, Brussels, Belgium. [8]These authors contributed equally: Edwige Martin-Valiente, Yao Du. e-mail: nicolas.baeyens@ulb.be

formation of large, fragile and prone-to-rupture arteriovenous shunts[5]. We hypothesized that different flow transduction signaling programs might be perturbed as congenital vascular anomalies are not restricted to BMP-related genetic mutations and develop in various vascular beds subjected to specific fluid forces. Therefore, genetic disturbance of different key mechanosensitive pathways would lead to different vascular defects in the vascular tree[7].

Vein of Galen aneurysmal malformations (VGAMs) are congenital arteriovenous fistulas draining to the median vein of the prosencephalon, or vein of Markowski, which is the vein of Galen embryonic precursor. Although rare, VGAMs are the most frequent cerebral arteriovenous shunts in neonates and infants[8]. Two major germline mutations have been reported in patients with VGAMs, with loss-of-function mutations in *RASA1* or *EPHB4* as the most prevalent lesions[9,10]. All the patients are heterozygous autosomal dominant carriers and often show other vascular malformations, regrouped in a series of clinical manifestations: capillary malformation–arteriovenous malformations (CM–AVMs)[11], the Parkes–Weber syndrome[12] and other fistulas. Several somatic mutations of *RASA1* have been reported, mostly in cutaneous lesions developing late in life[13]. Embolization by the trans-arterial route is the first (and only) line of treatment for VGAMs. In neonates, endovascular treatment is a high-risk procedure, and when possible, the child is medically treated for congestive heart failure (CHF), the main life-threatening complication. Untreated VGAMs have a poor prognosis and are almost always fatal, but it is equally important to recognize that surgical treatment is inappropriate in some cases[14,15]. If there is evidence of preexisting brain damage[16] (progressive atrophy or 'melting brain syndrome', parenchymal calcification) or severe multiorgan failure, a poor outcome, death or survival with severe brain damage is inevitable. Current clinical management of VGAMs has reached its limits, and there is an urgent need to understand the disease's etiology and identify complementary and supportive treatments.

For all these reasons, we sought to develop an in vivo model of VGAMs to characterize the cellular mechanism mediating its formation and determine the most appropriate pharmacological approach to stabilize or reduce VGAMs and CHF development in neonates. Previous studies by other teams have identified vascular remodeling defects in zebrafish larvae injected with antisense morpholinos against either *rasa1a* (ref. 17) or *ephb4a* (ref. 18), with the loss of *ephb4a* leading to the formation of fistulae in the dorsal longitudinal vein (DLV), reminiscent of the fistulae observed in patients with VGAMs[18].

Development of a clinically relevant animal model of VGAMs

VGAMs are clinically classified into two main types. The first one, 'choroidal', presents multiple high-flow fistulas and is the most complex manifestation, with a poorer prognosis. The second one, 'mural', is generally a single fistula generating a dilated median vein[19] (Fig. 1a).

We decided to use the zebrafish model to investigate the causality between the mutations and the formation of neurovascular defects. Indeed, the transparency and rapid neurovascular development of the zebrafish larvae make them models of choice to investigate vascular morphogenesis and blood flow dynamics in real time. First, we generated a *rasa1a* zebrafish mutant allele by CRISPR–Cas9-mediated genome editing, targeting a sequence in exon 2 of *rasa1a* (rasa1aulb28). In the mutant allele, a frameshift of 7 bp induces a premature stop codon, as observed in patients[10–12,20] (Extended Data Fig. 1a). Homozygous *rasa1a*$^{-/-}$ zebrafish can reach adulthood, although at frequencies lower than the one predicted by Mendelian genetics; have a smaller size than heterozygous *rasa1a*$^{+/-}$ or wild-type (WT) zebrafish; and are not fertile (Extended Data Fig. 1b). Second, we obtained an *ephb4a* mutant line from the Zebrafish International Resource Center (*ephb4a*^{hu3445}), in which a single point mutation in exon 4 leads to an early stop codon (Extended Data Fig. 1a). We exclusively used heterozygous mutants (*rasa1a*$^{+/-}$, *ephb4a*$^{+/-}$) and WT (*rasa1*$^{+/+}$, *ephb4*$^{+/+}$) zebrafish in our study, as the patients are also heterozygous. We did not observe cardiac edema in *rasa1a*$^{+/-}$ and *ephb4a*$^{+/-}$ larvae at 3 days postfertilization (dpf) and observed less than 15% cardiac edema at 5 dpf (Fig. 1b). We observed only a few heterozygous mutant larvae with minor intersegmental vessel (ISV) vascular growth defects at 5 dpf (Extended Data Fig. 2). Homozygous mutant larvae showed cardiac edema and ISV growth defects more frequently than the heterozygous mutant larvae at 3 dpf and 5 dpf (Fig. 1b and Extended Data Fig. 2). Therefore, heterozygous larvae have a more stable and uniform general phenotype than homozygous larvae and are fertile.

At 72 h postfertilization (hpf), both *rasa1a*$^{+/-}$ and *ephb4a*$^{+/-}$ mutants showed similar structural malformations of the DLV (Fig. 1c). We observed identical malformations of the DLV in *rasa1a* and *ephb4a* morphants. The vascular defects of *rasa1a* morphants could be partially rescued by *rasa1a* mRNA injections, showing the specificity of the morpholino phenotypes (Extended Data Fig. 3). The DLV belongs to the dorsal venous system as the vein of Markowski[21], the precursor of the vein of Galen, and sits above the diencephalon, mesencephalon and metencephalon. We therefore propose, as others did[18], that the DLV is a functional analog of the vein of Markowski[22]. After analyzing larvae from both heterozygous mutant lines, we describe two different structural defects of the DLV at 72 hpf: on one form, we observed the presence of dissociated vessels on the anterior segment, sometimes with dissociated vessels on the posterior segment (~40% of all *rasa1a*$^{+/-}$ larvae and ~30% of all *ephb4a*$^{+/-}$ larvae) (Fig. 1d). On the remaining heterozygous larvae (*rasa1a*$^{+/-}$ and *ephb4a*$^{+/-}$), not affected by a choroidal malformation, we observed a notably more dilated posterior segment of the DLV compared with WT larvae (Fig. 1c,e). So, heterozygous mutant larvae develop either choroidal malformations, mural malformations or no phenotype on the DLV, at 72 hpf. These two structural malformations are reminiscent of the two clinical forms of the disease described in human patients: the form with multiple vessels on both the anterior and posterior segments resembles a choroidal malformation with numerous fistulas. By contrast, the form with a dilated posterior segment resembles the mural malformation, with a dilation of the median vein.

Patients suffering from VGAMs often develop high-output heart failure[23], a critical factor for the survival of neonate patients affected by choroidal malformations. We examined the cardiac function of *rasa1a*$^{+/-}$ and *ephb4a*$^{+/-}$ larvae at 72 hpf. We observed a significant increase in the stroke volume, corroborated by an increase in atrium and ventricle volumes during diastole (Fig. 2a,b). We also observed increased blood flow velocity in the dorsal aorta (DA), reflecting the increased heart output (Fig. 2c). Therefore, both *rasa1a*$^{+/-}$ and *ephb4a*$^{+/-}$ mutants replicate the human disease's genetics and major cardiovascular tissue defects with neurovascular malformations (fistulas or dilation) in the dorsal venous system as well as increased cardiac output.

VGAMs result from a defective flow-mediated fusion

The existence of multiple, perfused and functional blood vessels in the malformation urged us to investigate its formation mechanism. We performed time-lapse imaging of the formation of the DLV in WT embryos. We observed a progressive fusion of two distinctly perfused precursor vessels within the first 4 h following 46 hpf. Then, we observed the elongation and constriction of the fused vessel in the next 4 h (Fig. 3a–c and Supplementary Video 1). Endothelial cells from distinct precursor vessels interact by direct contact before the fusion of the two precursor vessels (Supplementary Video 2). Initially, we observed the formation of a perfused donut-shaped structure. Cells then rearranged and migrated, fusing the donut and forming a collecting vessel with a single lumen; then, the blood vessel elongated and constricted to form the DLV itself.

https://doi.org/10.1038/s44161-025-00659-5

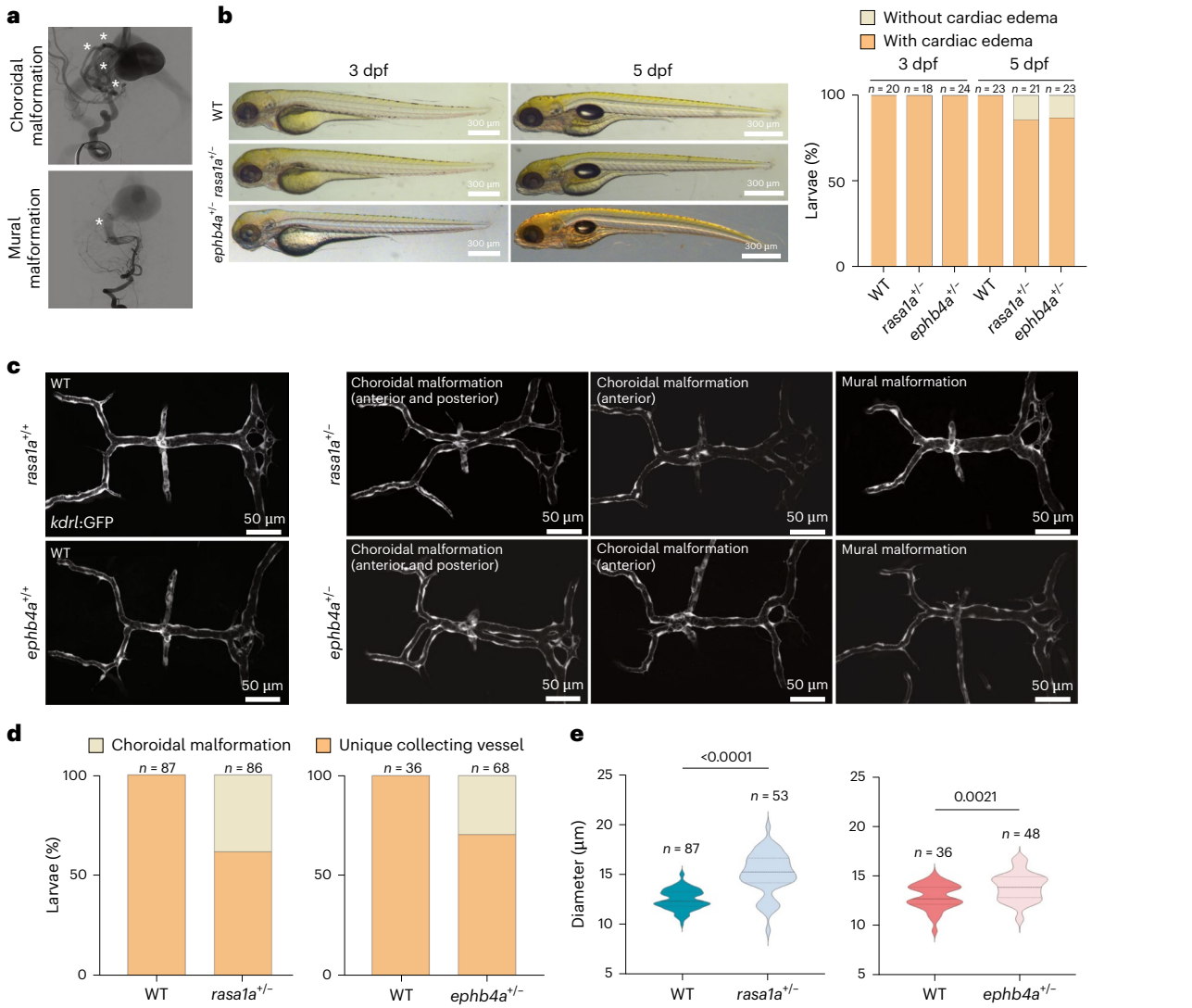

Fig. 1 | Development of *rasa1a* and *ephb4a* mutants as preclinical models of VGAMs. a, Digital subtraction angiography (Philips, Allura biplane system) frontal view of the right internal carotid artery and left vertebral artery showing a choroidal-type VGAM in the upper panel (patient: male, neonate, premature cesarian delivery at 38 weeks of pregnancy consecutive to decompensated heart failure) and a mural type in the lower panel (patient: male, 5 years old). **b**, Lateral views of WT (*rasa1a*$^{+/+}$ or *ephb4a*$^{+/+}$), *rasa1a*$^{+/-}$ and *ephb4a*$^{+/-}$ larvae at 3 dpf and 5 dpf. Quantification of cardiac edema in WT, *rasa1a*$^{+/-}$ and *ephb4a*$^{+/-}$ larvae at 3 dpf ($n = 20$ WT, $n = 18$ *rasa1a*$^{+/-}$ and $n = 24$ *ephb4a*$^{+/-}$) and 5 dpf ($n = 23$ WT, $n = 21$ *rasa1a*$^{+/-}$ and $n = 23$ *ephb4a*$^{+/-}$). **c**, Dorsal view of the DLV of WT (*rasa1a*$^{+/+}$ and *ephb4a*$^{+/+}$), *rasa1a*$^{+/-}$ and *ephb4a*$^{+/-}$ larvae at 3 dpf. **d**, Quantification of the percentage of choroidal malformations ($n = 87$ WT, $n = 86$ *rasa1a*$^{+/-}$ and $n = 36$ WT, $n = 68$ *ephb4a*$^{+/-}$). **e**, Quantification of the diameter of the posterior segment in larvae with no choroidal malformation ($n = 87$ WT, $n = 53$ *rasa1a*$^{+/-}$) in *rasa1a*$^{+/-}$ larvae and ($n = 36$ WT, $n = 48$ *ephb4a*$^{+/-}$) in *ephb4a*$^{+/-}$ larvae at 3 dpf (Mann–Whitney *U* test; *P* values are indicated on the graph).

The *rasa1a*$^{+/-}$ embryos show an ineffective vessel fusion process, developing distinct vessels (Fig. 3a–c and Supplementary Video 3). Indeed, the cells from the precursor vessels do not interact and fuse, as observed in the WT embryos. The distinction between the mural and choroidal malformations, described in Fig. 1, most probably stems from which step of the DLV formation process (cell–cell interaction and fusion versus constriction and elongation of the fused vessel) is ineffective. The absence of cell–cell contact, cell reorganization and fusion of the initial donut-shaped structure leads to choroidal malformations with multiple fistulas in both the anterior and posterior portions of the dorsal venous system, as the precursor vessels that did not fuse further developed as perfused fistulas (Fig. 3d). However, defective constriction of the fused vessels at later stages develops into a mural malformation. Both are distinct phenotypes. The fusion process requires that some endothelial cells, at the interface of two joining vessels (arrow, Fig. 3c), perceive and integrate mechanical stimuli generated from the two pulsatile bloodstreams for the fusion to be successful, with blood flow mechanotransduction as a potentially important driver of the fusion process.

Therefore, we assessed whether blood flow contributed to DLV development in WT and mutant zebrafish. We observed that the preliminary vascular structure leading to the formation of the DLV was already perfused at 36 hpf (Extended Data Fig. 4a) and that the choroidal malformation consists of perfused fistulas (Fig. 3d). These data show that blood flow is present before DLV formation and might contribute as a mechanical stimulus to the development of the DLV. We used two different approaches to gain insight into the role of flow in this specific vascular development program. First, we stopped blood flow by injecting a morpholino targeting cardiac troponin T (*tnnt2a*) at a low concentration (0.25 ng µl^{-1}) to stop the heartbeat from the beginning of the cardiovascular development, with no blood flow within the vascular system of the developing embryo[24]. While most of the zebrafish embryo

https://doi.org/10.1038/s44161-025-00659-5

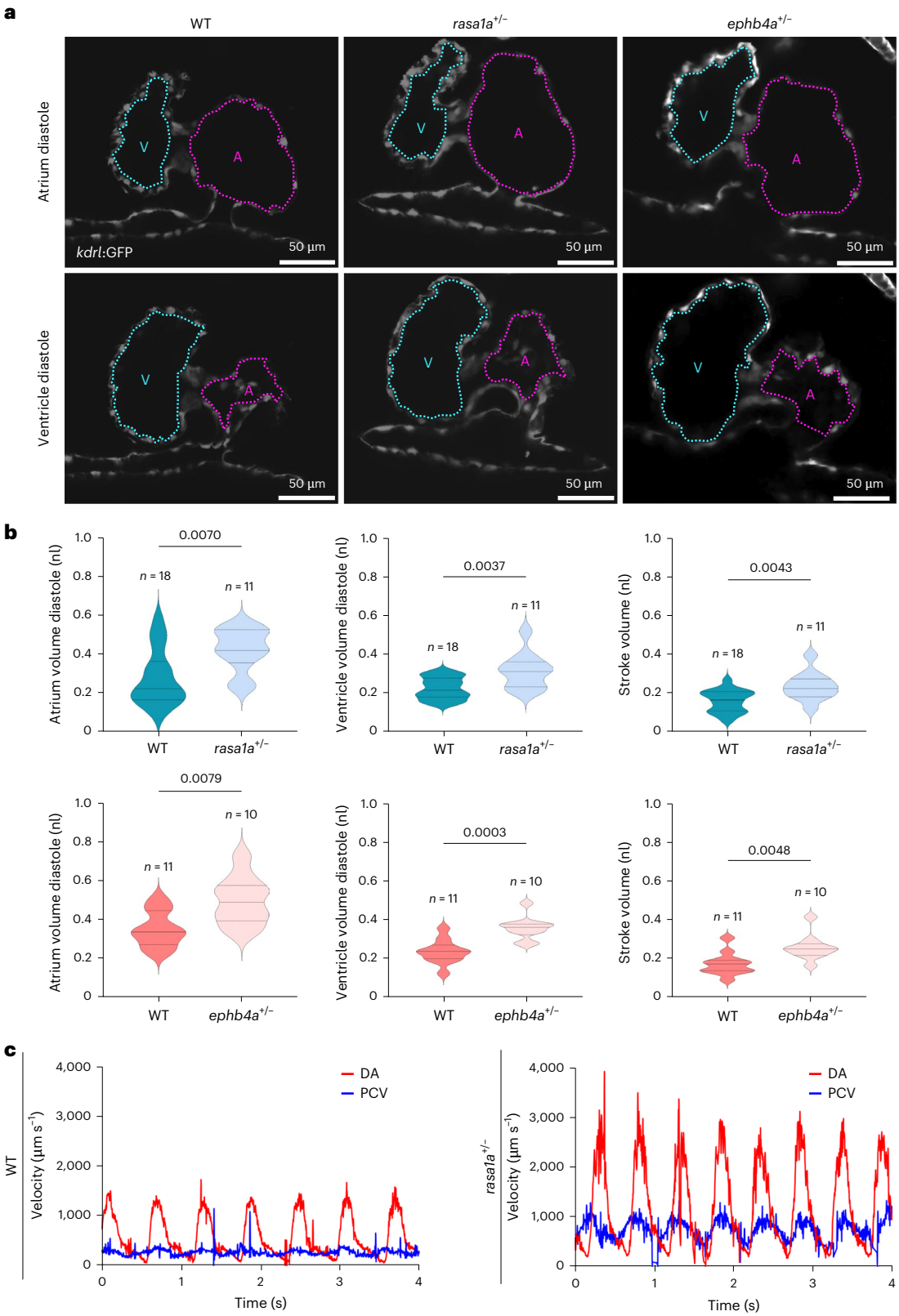

Fig. 2 | Characterization of the cardiac function of *rasa1a* and *ephb4a* mutants. a, Acquisition of the *Tg(kdrl:GFP)* heart cycle of WT, *rasa1a*$^{+/-}$ and *ephb4a*$^{+/-}$ larvae at 3 dpf. The atrium (A) is outlined in magenta and the ventricle (V) in cyan during systole and diastole. **b**, Quantification of the volume of atrium diastole and ventricle diastole and stroke volume ($n = 18$ WT, $n = 11$ *rasa1a*$^{+/-}$ and $n = 11$ WT, $n = 10$ *ephb4a*$^{+/-}$) at 3 dpf (Mann–Whitney *U* test). **c**, Velocity of red blood cells in the DA and the PCV at 3 dpf for WT and *rasa1a*$^{+/-}$ larvae.

https://doi.org/10.1038/s44161-025-00659-5

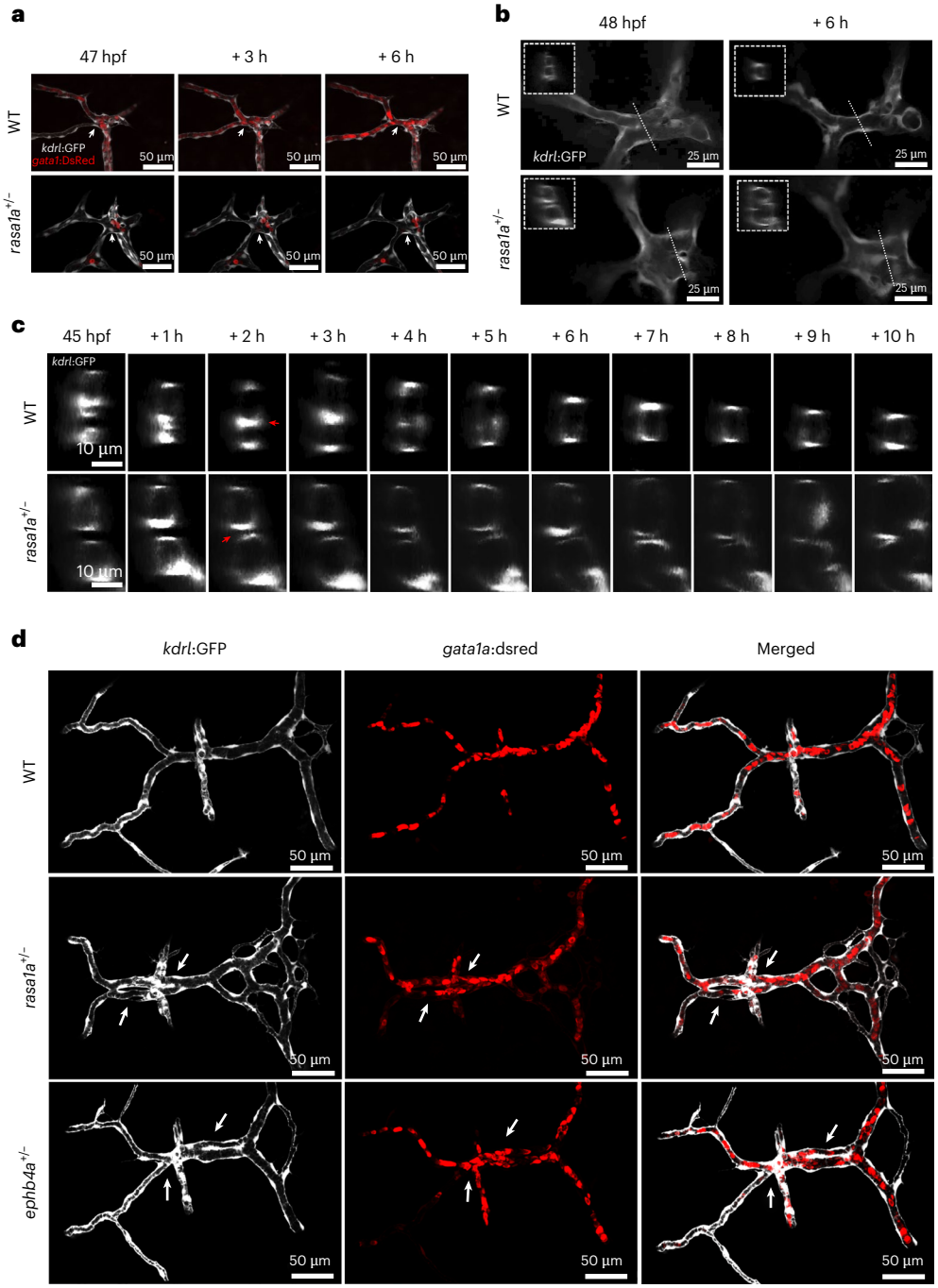

Fig. 3 | VGAMs are consecutive to a fusion and constriction failure during the development of the collecting vessel. a, Maximum projection of the vessels and the red blood cells of WT and *rasa1a*$^{+/-}$ in *Tg(kdrl:GFP);(gata1a:DsRed)* double transgenics. The white arrows indicate the perfusion of two different streams to become one for WT larvae, while remaining as two separate streams in *rasa1a*$^{+/-}$ larvae. **b**, Observation of the formation of the anterior segment of the DLV at 48 hpf and 54 hpf (collecting vessel, white square: transversal section at the location of the dashed line). **c**, Time-lapse observation of the formation of the anterior segment of the DLV (collector vessel in WT and *rasa1a*$^{+/-}$), transversal section. The red arrows show the lumen total fusion for the WT and the partial one for the mutant. **d**, Maximal intensity projection of the dorsal view of the DLV of WT, *rasa1a*$^{+/-}$ or *ephb4a*$^{+/-}$ larvae with a choroidal malformation at 3 dpf. The white arrows indicate two perfused vessels on the anterior and two perfused vessels on the posterior segment of the DLV.

vascular system develops as it should from a structural point of view (Fig. 4a), as flow is not entirely required for its primary development[25], we observed a complete lack of development of the DLV (Fig. 4b) of both WT and mutant embryos. Indeed, in embryos of both genotypes, the DLV remained entirely undeveloped with no fusion or elongation of the precursor vessels, indicating that both the formation of the normal DLV and the malformations in mutant embryos require blood flow to form. We confirmed this observation with a second experiment, in which we incubated the embryos in 0.65 mg ml^{-1} of tricaine right before the beginning of the fusion process at 47 hpf, stopping blood circulation only right before this crucial step. As observed with *tnnt2a* morpholinos, blocking blood flow pharmacologically impaired the development of the DLV (Fig. 4c). As expected, overexpression of *rasa1a* by mRNA injections could not rescue DLV development without flow, as blood flow is a mechanical stimulus involving a wide array of mechanosensors and signaling cascades (Extended Data Fig. 4b).

https://doi.org/10.1038/s44161-025-00659-5

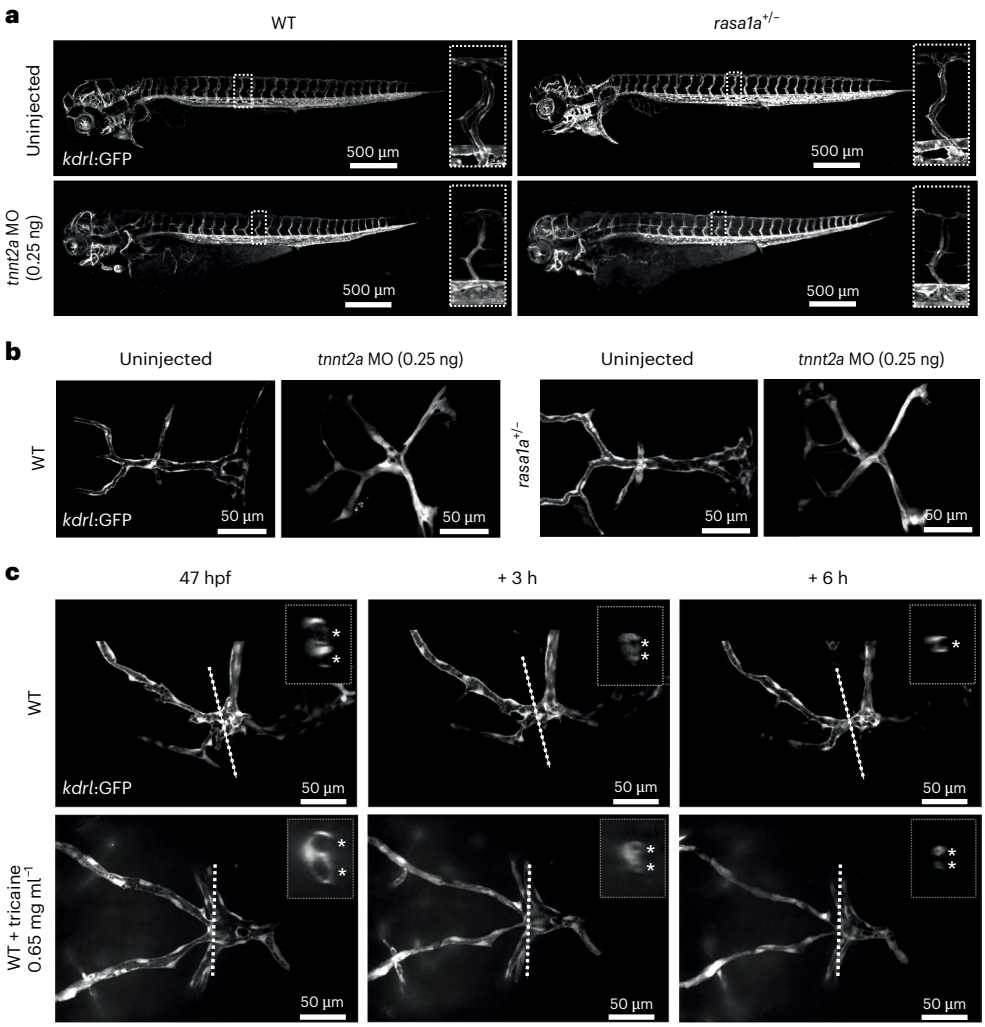

Fig. 4 | Rasa1 contributes to the formation of collecting vessels through a flow-mediated fusion of immature vessels. a, Lateral views of WT and *rasa1a*$^{+/-}$ embryos injected with 0.25 ng *tnnt2a* morpholino, at 3 dpf (white square: magnification of the ISV). **b**, DLVs of WT and *rasa1a*$^{+/-}$ embryos injected with 0.25 ng *tnnt2a* morpholino at 3 dpf. **c**, Stills of a time-lapse recording of WT DLV formation with and without tricaine overdose (0.65 mg ml^{-1}) (the white square is a transversal section at the location of the dashed line, and the number of asterisks indicate the number of distinct vessels).

We also counted the number of endothelial cells, as an increased cell number could be required to induce additional vessels in choroidal malformations. The analysis of the number of stained nuclei in the *kdrl:nls.cherry* transgenic line did not reveal a significant difference in the number of endothelial cells in the DLV of the WT compared with the DLV with a choroidal malformation and multiple perfused vessels in *rasa1a*$^{+/-}$ mutants (Extended Data Fig. 4c).

The DLV is a collecting vessel

We observed stable, perfused fistulae in the DLV of *rasa1a*$^{+/-}$ and *ephb4a*$^{+/-}$ mutants, with no similar defects observed elsewhere in the systemic vasculature (Extended Data Fig. 2). We then decided to characterize the hemodynamic properties of this vascular bed more precisely and compare them with those of other systemic vessels. Tracking red blood cell velocities extrapolated the hemodynamic parameters within the blood vessels of zebrafish. We observed a pulsatile flow with high shear stress in the DA and a non-pulsatile flow with low shear stress in the posterior cardinal vein, as expected for an artery and a vein (Fig. 5a). Interestingly, we measured a pulsatile flow with high shear stress in the DLV, almost similar to what is observed in the DA and much higher than what is observed in the posterior cardinal vein (PCV) (Fig. 5c). Frequency analysis of the pulsatility in the DA determined a fundamental harmonic of 1.8 Hz, corresponding to the frequency of the beating heart. In comparison, the fundamental harmonic of the DLV was doubled at 3.8 Hz (Fig. 5b). This surprising result led us to analyze the behavior of single red blood cells. We individually tracked red blood cells from each incoming vessel and labeled their tracks with a distinctive color for each inlet (green for the top and red for the bottom in the case of Fig. 5d). It revealed independent tracks that were restrained to the side of each entry along the DLV as if they could not cross an imaginary border at the vessel's center. This observation shows the existence of streams of red blood cells within the DLV, which acts as a collecting channel where streams do not mix. As they do not mix, these streams possess their characteristics regarding pulsatility and, most likely, pressure and other hemodynamic parameters.

High-flow AVMs are frequently observed in two distinct congenital syndromes: HHT syndrome characterized by loss-of-function genetic mutations affecting BMP signaling[26] and CM–AVMs with loss-of-function genetic mutations affecting *RASA1* (ref. 12) or *EPHB4* (ref. 20). Interestingly, HHT malformations mainly develop in specific vascular networks[27] (brain, liver, lung, mucosae of the digestive system and the superficial vascular network of the dermis). Similarly, CM–AVMs have been described to develop in distinct vascular beds than HHT-related AVMs, namely, in the skin's deep vascular network,

https://doi.org/10.1038/s44161-025-00659-5

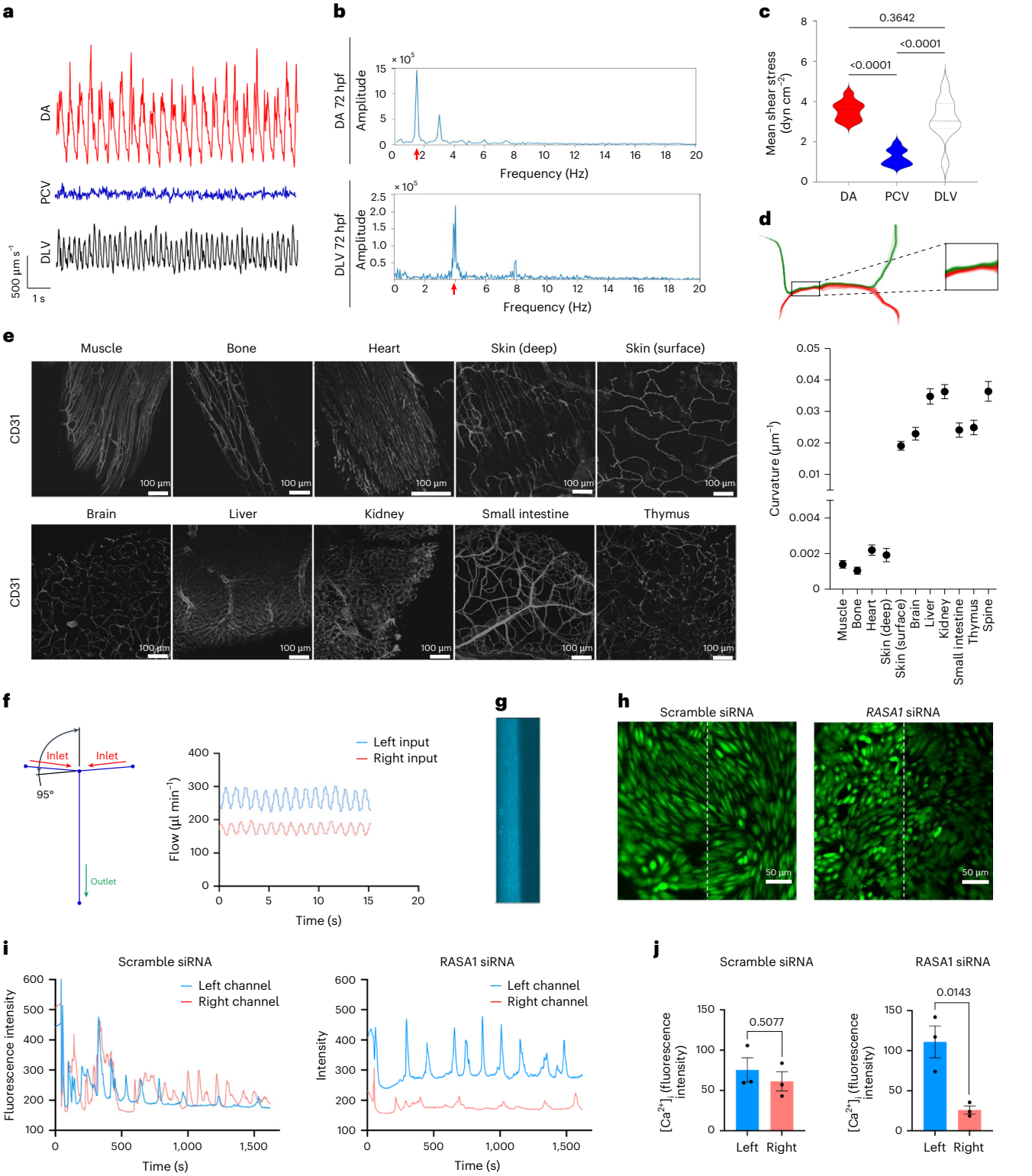

Fig. 5 | Analysis of blood flow and mechanosensation in a collecting channel. **a**, Velocity of red blood cells in the DA, the PCV and the DLV. **b**, Frequency analysis by Fourier transform of red blood cell velocity. The red arrows show the fundamental harmonic. **c**, Estimation of fluid shear stress intensities in each vessel ($n = 10$, one-way analysis of variance (ANOVA) with Tukey posttest; P values are indicated in the graph). **d**, Analysis of the trajectory of red blood cells originating from the top left entry (green) or the bottom left entry (red). **e**, Analysis of the curvature of capillaries in various cleared organs from mice with the immunolabeling-enabled three-dimensional imaging of solvent-cleared organs protocol and stained for CD31. The graph on the right shows the average curvature (mean ± s.e.m.) for each tissue. Number of capillaries measured: brain, 100; muscle, 36; bone, 14; heart, 32; liver, 75; kidney, 82; deep skin, 31; skin surface, 36; intestine, 38; spine, 46; and thymus, 45. **f**, Description of the flow chamber and representative flow measures injected in each inlet. **g**, Capture of the channel within the flow chamber. The left inlet has been perfused with fluorescent blue beads, and the right inlet has non-fluorescent water. **h**, Representative images of intracellular calcium with a calcium reporter (Calbryte-520 AM) 25 min after applying flow on HUVECs transfected with a scramble or a *RASA1* siRNA; the experiment was repeated three times. **i**, Intracellular calcium measurements in HUVECs transfected with a scramble or *RASA1* siRNA. One representative calcium trace is shown over 30 min from the collecting channel's left or right side. **j**, Histograms of the average intensity of calcium oscillation (three separate experiments, unpaired t-test, mean ± s.e.m.).

musculoskeletal vascular networks and the developing vein of Galen[28]. We hypothesized that CM–AVMs develop in different vascular beds than AVMs of patients with HHT, possibly owing to a different structural organization and blood flow profiles within those respective vascular beds. We performed volumetric imaging of several mouse organs to compare the architecture of their vascular networks and identify possible common structural features among them. Strikingly, capillaries from muscles (cardiac or skeletal), bone and the deep vascular network of the dermis, where CM–AVMs preferentially develop in patients, shared a common structural feature: they consist of straight, elongated, collecting vessels with a similar architecture to the one observed in the DLV. Contrastingly, capillary networks of the brain, the superficial layer of the dermis, the kidney, the liver, the small intestine and the thymus, where HHT-related malformations develop, showed pronounced curvature of their capillaries (Fig. 5e). Curvature analysis of these capillaries revealed two very distinctive groups, with more than an order of magnitude of difference for the curvature of the capillaries between HHT and CM–AVM-associated capillary beds (Fig. 5e). This difference suggests that the formation of those distinct capillary networks might stem from different angiogenesis programs and that hemodynamics would differ in each group to fulfill a different function. It is well known that curves in microscopic vessels generate centrifugal forces, which cause secondary flow vortices[29], allowing the fluid to be mixed. By contrast, straight vessels similar to the DLV might have different streams with poor mixing, a well-known issue in microfluidics[30].

Rasa1 contributes to mechano-adaptation to heterogenous flow

Blood flow mechanotransduction involves numerous receptors and signaling pathways[4,7,31]. To investigate the contribution of Rasa1 to blood-flow sensing, we developed a simplified in vitro polydimethysiloxane model of the DLV, with a collecting channel perfused by two orthogonal inlets that can be perfused independently. We perfused the left inlet with a pulsatile flow of higher magnitude than the right inlet (Fig. 5f), generating two fluid streams with distinct properties that do not mix inside the collecting channel, as observed in the DLV of the zebrafish larva (Fig. 5g). Despite two streams with different mechanical parameters and different mechanical stimulation across the channel, WT cells transfected with a scramble small interfering RNA (siRNA) showed a uniform calcium response in the left and right portions of the channel 25 min after the flow application, indicating that the endothelial cell monolayer responded uniformly to a nonhomogeneous mechanical stimulation, mitigating the differences (Fig. 5h–j and Supplementary Video 4). Consequently, endothelial cells can be subjected to different mechanical stimuli, which can be perceived and integrated to make the response uniform across a monolayer within a vessel through cell–cell communication. Strikingly, cells deficient in RASA1 showed a sharply different response on the left and right portions of the channel (Fig. 5h–j and Supplementary Video 5). Calcium response is markedly and significantly higher in the left portion of the channel than in the right portion. Therefore, as a flow-sensitive organ, the endothelial monolayer is separated into two distinctive portions when Rasa1 expression is depleted. This indicates that Rasa1 contributes to flow-mediated cell–cell communication in an endothelial cell monolayer.

When organized in a monolayer, endothelial cells subjected to physiological laminar flow will align in the flow direction[32], a unique endothelial cell feature associated with endothelial homeostasis[4]. We observed that human umbilical vein endothelial cells (HUVECs) transfected with an siRNA against *Rasa1* do not lose their ability to sense flow direction and to align in the flow direction, just as normal cells (Fig. 6a). Therefore, RASA1 specifically modulates only some aspects of the response to flow. Numerous signaling pathways are transduced in response to flow, including phosphatidylinositol-3-kinase (PI3K) and extracellular signal-regulated kinase (ERK) signaling. These two signaling cascades are known to be downstream of Rasa1 in response to chemical agonist stimulation, as Rasa1 is a Ras GTPase activating protein[33]. Therefore, we measured how Rasa1 knockdown would affect the flow-mediated activation of Akt and ERK. First, we measured how *rasa1* knockdown affects vascular endothelial growth factor (VEGF)-mediated activation of ERK and Akt, as VEGF is known to activate both pathways during angiogenesis[34]. As depicted in Fig. 6b, we could not observe any significant difference between cells transfected with a scramble siRNA and cells transfected with *Rasa1* siRNA in response to VEGF stimulation (uncropped gels in Supplementary Fig. 1).

However, Rasa1 knockdown cells showed defective flow-dependent activation of ERK, and Akt: ERK phosphorylation was slightly potentiated, while Akt phosphorylation by PI3K was significantly reduced after flow (Fig. 6c and uncropped gels in Supplementary Fig. 2). This contrasts with cells transfected with a scramble siRNA, in which Akt and ERK are activated after applying flow, although with different kinetics. This observation confirms the specific involvement of Rasa1 signaling in flow mechanotransduction. It provides ground for attempting to correct pharmacologically the inadequate response to flow and, potentially, the defective flow-mediated fusion of immature vessels.

Targeting PI3K/MEK signaling reverses malformations

We hypothesized that correcting the imbalance in flow activation of PI3K/ERK signaling would restore proper vessel fusion and constriction in the mutants. We treated WT, *rasa1a*$^{+/-}$ or *ephb4a*$^{+/-}$ zebrafish with either DMSO (used as a solvent), selumetinib (MEK1 inhibitor[35], targeting ERK activation, 1 µM), YS-49 (PI3K activator[36], restoring Akt activation, 1 µM) and a combination of selumetinib and YS-49 (1 µM each). We deployed two protocols to assess whether pharmacological treatment would restore DLV structure and mitigate the development of the malformation. The first protocol (Fig. 7a) consisted in incubating the drugs from 36 hpf to 60 hpf, during the development of the DLV. We measured a significant reduction of the diameter of the DLV, with an increasing effect from selumetinib, YS-49 and then the combination of both drugs until returning to the values measured in WT zebrafishes (Fig. 7b). We observed a reduction in the proportion of *rasa1a*$^{+/-}$ larvae showing choroidal malformations (40% with DMSO) after using either selumetinib (25%) or YS-49 (20%) (Fig. 7c). Combining both drugs did not improve the outcome compared with using a single drug. In *ephb4a*$^{+/-}$ larvae, we also observed similar results for the reduction of DLV diameter but the drugs were less efficient in reducing the number of larvae with choroidal malformations (Fig. 7b,c). This experiment validates the hypothesis that a defective flow-mediated activation of MAPK and PI3K signaling contributes to malformation development.

We then tested whether the drugs might reverse the two malformations as a potential therapeutic approach. To test this, we treated larvae with the different drugs at 72 hpf for 24 h, when the malformation was fully formed, and monitored the drugs' effect on the mural or choroidal malformations after 24 h (Fig. 8a).

Interestingly, choroidal malformations remained stable from 72 hpf to 96 hpf in the absence of treatment (DMSO), highlighting the stability of these fistulae. The administration of either selumetinib or YS-49, or the combination of both, reversed the choroidal malformation in nearly 50% of the treated *rasa1a*$^{+/-}$ larva, with a more marked effect of YS-49 (Fig. 8b). The impact of the drugs was more pronounced on *ephb4a*$^{+/-}$ larvae, with more than 50% of larvae restoring vessel fusion with either selumetinib or YS-49 and 75% of larvae with a combination of both molecules (Fig. 8b). It is, therefore, possible to trigger the fusion of established choroidal malformations.

The drugs' impact on enlarged mural malformations in *rasa1a*$^{+/-}$ or *ephb4a*$^{+/-}$ larvae was also positive when using selumetinib, YS-49 or the combination of both molecules (Fig. 8c), as we could measure a significant reduction of the diameter of the enlarged DLV. This suggests

https://doi.org/10.1038/s44161-025-00659-5

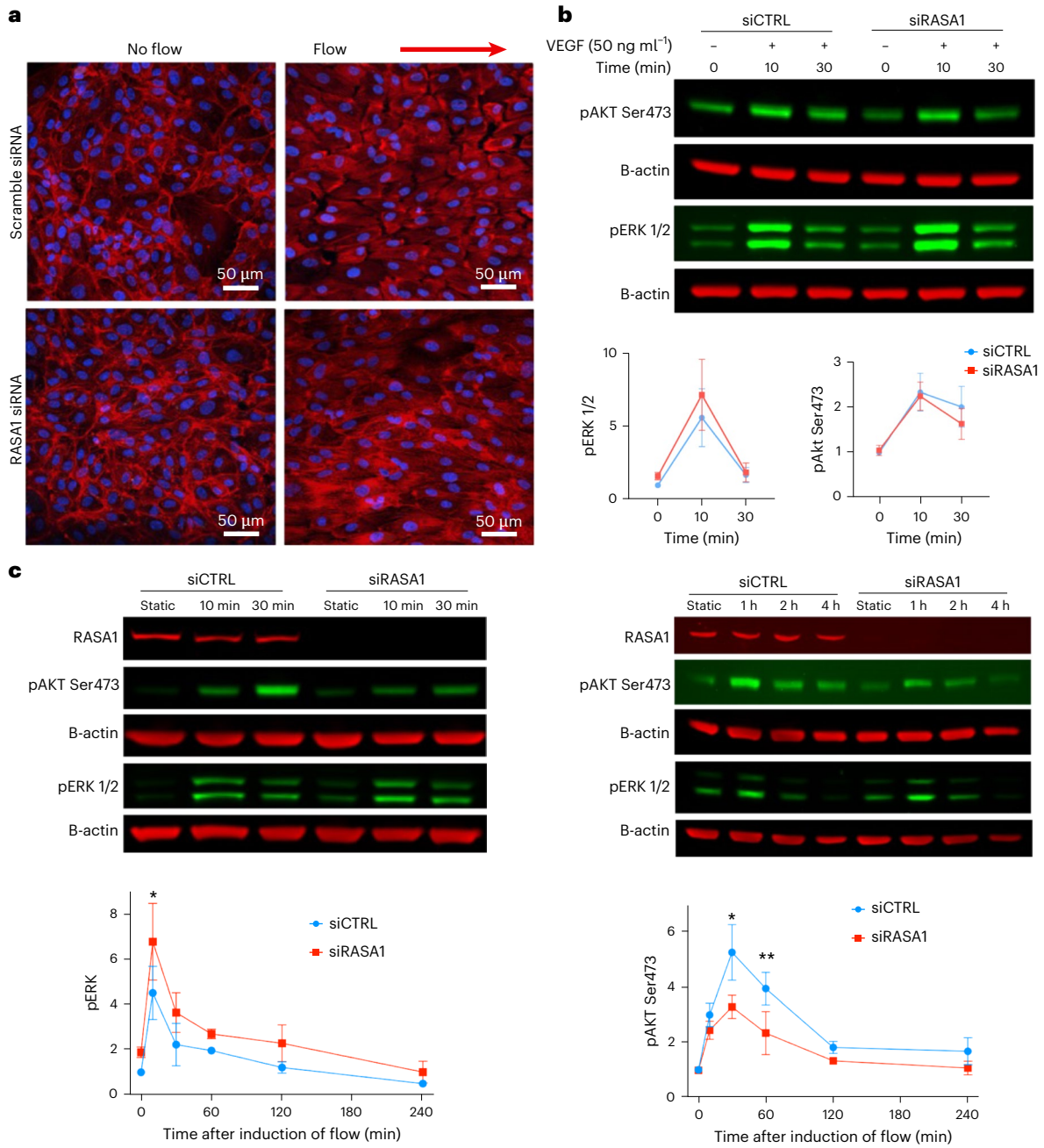

Fig. 6 | Identification of impaired flow mechanotransduction responses. **a**, Endothelial cell monolayer organization after 16 h of laminar flow (12 dyn cm^{-2}) applied on HUVECS transfected with a scramble or *RASA1* siRNA; the arrow indicates the direction of flow. Cells were stained for f-actin with phalloidin (red) and the nuclei with DAPI (blue); the experiments were repeated three times. **b**, Western blot of ERK1,2 (Thr202/Tyr 204) and Akt phosphorylation (Ser473) in response to VEGF (50 ng ml^{-1}) for 0 min, 10 min and 30 min (3 independent experiments, ANOVA, Sidak multiple-comparison posttest, mean ± s.e.m.). **c**, Western blot of ERK1,2 (Thr202/Tyr 204) and Akt phosphorylation (Ser473) in response to laminar flow (12 dyn cm^{-2}) for 0 min, 10 min and 30 min, 1 h, 2 h and 4 h (aggregate of 3 separate experiments for each time point, ANOVA, Sidak multiple-comparison posttest, mean ± s.e.m., *$P < 0.05$, **$P < 0.01$).

that the constrictive process could also be restored in enlarged mural malformations.

Discussion

Vascular remodeling is an essential feature of vascular embryogenesis and homeostasis. Flow mechanosensing is one of the main drivers of lumen formation[37], vascular remodeling and vessel homeostasis[38], yet the specific nature of mechanosensing programs still needs to be better understood and mapped out. We know that the nature of the flow within a developing vessel will determine the nature of the remodeling program[4,7,31]. Pruning of lowly or non-perfused, immature capillaries redirects endothelial cells toward perfused areas[1,39]. However, forming pillars within a developing lumen, a process called intussusception, requires low perfusion to stabilize the pillar[40]. Then, it has been observed that highly perfused capillaries could undergo reverse intussusception or, simply put, fuse[41]. This later process, the flow-mediated fusion of immature vessels, has been directly linked to vascular endothelial-cadherin (VE-cadherin) activation[42], a cell–cell transmembrane receptor contributing to a major flow mechanosensory complex[43] and endothelial cell homeostasis. Still, this mechanism cannot explain the specific nature of the flow-mediated fusion of immature vessels, as VE-cadherin phosphorylation is also observed in other

https://doi.org/10.1038/s44161-025-00659-5

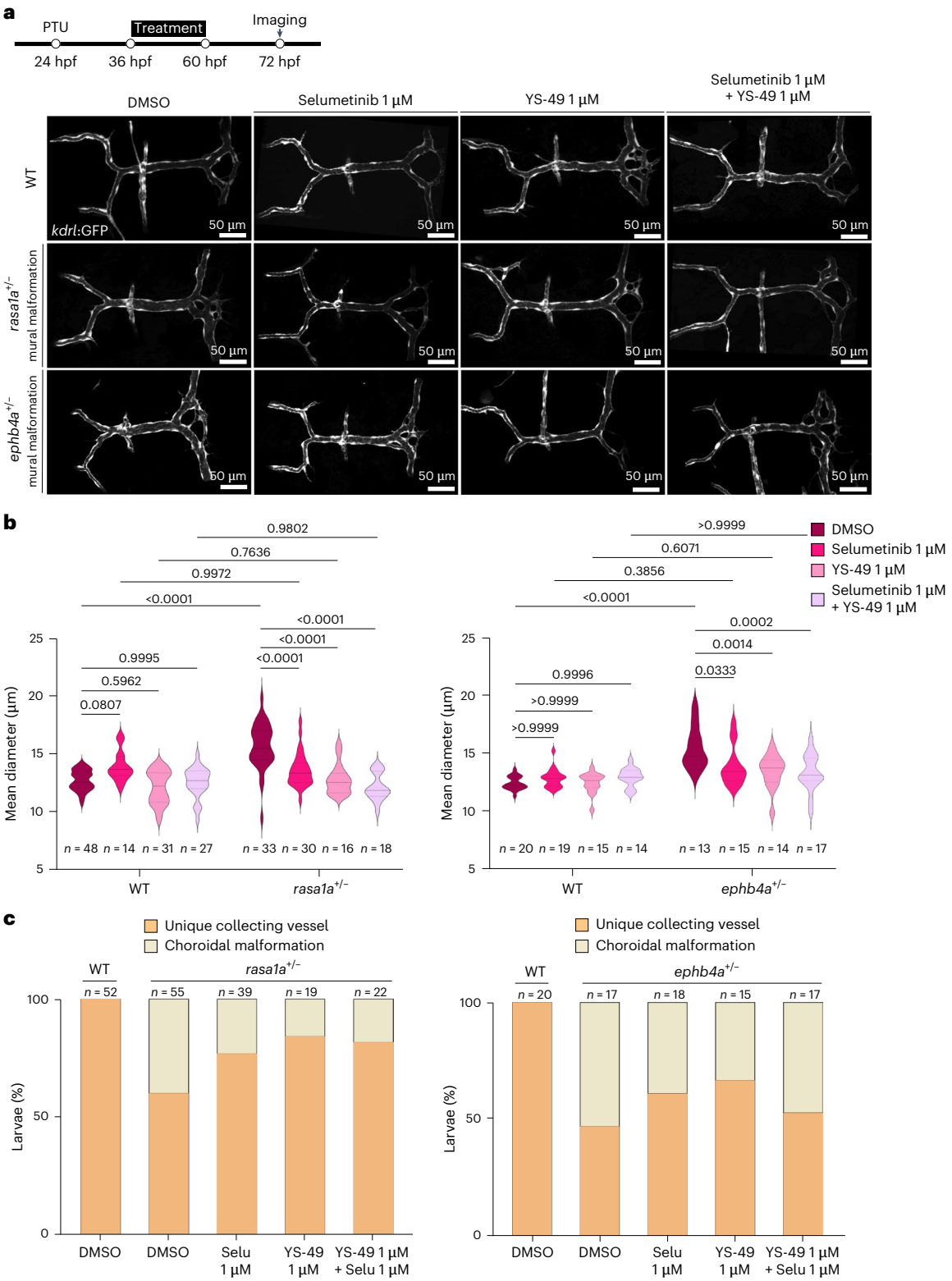

Fig. 7 | Pharmacological modulation of the PI3K or MAPK pathways prevents DLV malformations in *rasa1a*$^{+/-}$ and *ephb4a*$^{+/-}$. **a**, Effect of the inhibition of ERK signaling (selumetinib 1 µM) or activation of PI3K (YS-49 1 µM) or a combination of both during the development of the DLV (36–60 hpf). Maximum projection of the DLV of *Tg(kdrl:GFP)* WT, *rasa1a*$^{+/-}$ and *ephb4a*$^{+/-}$ DLV with a mural malformation before and after the pharmacological treatment. Selu, selumetinib. **b**, Quantification of the average diameter of mural malformation after the pharmacology treatment of the WT, *rasa1a*$^{+/-}$ and *ephb4a*$^{+/-}$ larvae (left graph: WT DMSO, $n = 48$; *rasa1a*$^{+/-}$ DMSO, $n = 33$; WT selumetinib, $n = 14$; *rasa1a*$^{+/-}$ selumetinib, $n = 30$; WT YS-49, $n = 31$; *rasa1a*$^{+/-}$ YS-49, $n = 16$; WT selumetinib + YS-49, $n = 27$; and *rasa1a*$^{+/-}$ selumetinib + YS-49, $n = 18$; right graph: WT DMSO, $n = 20$; *ephb4a*$^{+/-}$ DMSO, $n = 13$; WT selumetinib, $n = 19$; *ephb4a*$^{+/-}$ selumetinib, $n = 15$; WT YS-49, $n = 15$; *ephb4a*$^{+/-}$ YS-49, $n = 14$; WT selumetinib + YS-49, $n = 14$; and *ephb4a*$^{+/-}$ selumetinib + YS-49, $n = 17$). **c**, Quantification of the percentage of choroidal malformation after the pharmacology treatment of the WT, *rasa1a*$^{+/-}$ and *ephb4a*$^{+/-}$ larvae (left graph: WT DMSO, $n = 52$; *rasa1a*$^{+/-}$ DMSO, $n = 55$; *rasa1a*$^{+/-}$ selumetinib, $n = 39$; *rasa1a*$^{+/-}$ YS-49, $n = 19$; *rasa1a*$^{+/-}$ selumetinib + YS-49, $n = 22$; right graph: WT DMSO, $n = 20$; *ephb4a*$^{+/-}$ DMSO, $n = 17$; *ephb4a*$^{+/-}$ selumetinib, $n = 18$; *ephb4a*$^{+/-}$ YS-49, $n = 15$; *ephb4a*$^{+/-}$ selumetinib + YS-49, $n = 17$). Statistical analysis: two-way ANOVA with multiple comparisons.

flow-dependent remodeling programs[44] and because VE-cadherin phosphorylation directly affects endothelial junction formation and, therefore, the formation of the junctional mechanosensor, a primum movens in flow mechanotransduction.

Working with an animal model that is RASA1 or EPHB4 deficient has proven difficult, as seen in the embryonic lethality of the knockout mice[45,46]. The two zebrafish mutants used in this study recapitulate the phenotype observed in *ephb4* (ref. 18), with the generation of fistulae in the dorsal venous system of the cerebral vasculature. We reproduced these results by using morpholinos targeting *rasa1a* or *ephb4a*. Another group has generated multiple *rasa1a* and *rasa1b* (ref. 47) mutant alleles but did not describe the DLV morphology. Yet, they described malformations of the caudal venous system at an earlier stage of the larval development in double *rasa1a/rasa1b* mutants.

Our study provides further evidence for vessel fusion as the necessary process to form collecting vessels that drain multiple high-flow feeding vessels. The existence of different mechanical stimuli during the fusion process necessitates an integration and adaptation of the endothelial cells, which would have to act as a single tissue despite the differences across the monolayer. In the absence of Rasa1, cells cannot mitigate multiple mechanical signals from blood flow, reinforcing the stabilization of multiple single fistulas rather than the formation of a single collecting vessel by fusion. Failure to fuse could also be explained by a defective flow-dependent cell–cell communication, maybe through EphB4, the other mutated gene in VGAMs[20] or a defective flow-mediated signaling cascade. Indeed, calcium waves cannot propagate anymore across the endothelial monolayer. The exact molecular culprit remains to be identified. Others have proposed a defective collagen IV secretion, which might contribute to the stabilization of the fused vessel[48].

We also describe specific vascular beds where such collecting vessels are present, namely, musculoskeletal capillaries, deep dermal capillaries, the vein of Markowski and myocardial capillaries. The developmental program of these vessels most probably involves flow-dependent vessel fusion, as we could not observe any development of the DLV in the absence of perfusion of the developing vascular network and because those vessels share structural features with the DLV and are frequently associated with lesions in CM–AVM syndrome. Many vascular diseases have been linked to specific flow-sensing mechanisms: atherosclerosis develops in areas of multidirectional flow, and from a defective perception of flow direction[32,49], HHT-associated AVMs result from a defective flow-mediated stabilization of vessel development[5,50,51], inward remodeling and hypertensive diseases to low-flow sensing[52,53]. Our study provides evidence for a pathological consequence of a defective flow-mediated fusion angiogenic program. Therefore, it identifies Rasa1 and EphB4 as important molecular actors of this poorly understood physiological mechanism in angiogenesis. Interestingly, another group has reported vascular anomalies in the adult myocardial vascular network of the mouse but not the skeletal muscle after an endothelial-specific deletion of EphB4 (ref. 54).

Flow properties vary across the vascular system and depend highly on the local architecture. At the microvascular level, fluid flow is affected by architectural factors such as curvature[29] and the nature of blood as a fluid[55], and, therefore, we might postulate that physics within capillaries is different from physics in larger vessels. Further studies must be conducted to appreciate the exact nature of biomechanics within capillaries fully. We identified two subgroups of microvascular networks differentiated by their curvature, which correlate with the localization of lesions either in CM–AVMs or HHT syndromes, indicating that flow properties and geometrical characteristics of the affected vascular network are probable contributors to the location of a lesion. Furthermore, it shows that mechanotransduction pathways are differentially activated and impacted based on the different hemodynamics or genetic anomalies, explaining the differences across vascular remodeling defects in disease.

Clinically, VGAMs are occasionally detected on antenatal ultrasound scans (from about 25 weeks of gestation). More commonly, VGAMs are diagnosed at birth. Often, delivery and the first 24 h are unremarkable. More significant shunts may rapidly deteriorate with progressive CHF, leading to multiorgan failure. Occasionally, children present later in childhood with macrocrania or prominent facial veins secondary to venous outflow obstruction. Embolization is the first line of treatment for VGAMs and is usually performed in several sessions with glue (liquid embolic agent). A good outcome is anticipated when this treatment is performed before significant brain damage has occurred. In a recent meta-analysis[19], the result was favorable in 68% of patients and unfavorable in 31%, with a mortality rate of 16%. The worst prognosis was seen, as expected, in babies with the largest shunts, presenting as neonates with severe high-output heart failure. Despite improvements in endovascular technologies and neonatology, these results compare unfavorably with those obtained in older children and adults with arteriovenous shunts. Moreover, a recent study has shown that long-term outcomes are less favorable than short- and mid-term outcomes, even without encephalomalacia at birth[19]. These patients will develop neuropsychological disorders and neurodevelopmental alterations. Therefore, current VGAM management has significant limitations in patients with a severe clinical presentation, and there is a need for potential pharmacological support to decrease the potential brain parenchymal destruction by venous hyper-pressure, decrease CHF, increase the success rate of endovascular procedures and reduce the late neurodevelopmental alterations. We identified PI3K activators and MAPK inhibitors as potential pharmacological modulators of VAGM formation. Interestingly, PI3K activators, in particular, could reverse an already stably formed choroidal lesion, providing preclinical evidence for a combinatory therapeutical approach in managing VGAMs with a poor prognostic. This pharmacological modulation is also supported by data from a previous study[47]. This shows that ERK inhibition reduces the phenotype observed in the caudal venous plexus[47]. Stabilizing neonates pharmacologically should now be considered, and it could positively support their development until they are strong enough to undergo an endovascular procedure.

Improving the care of these neonates required a deeper understanding of the etiology, which needed the contribution of various disciplines. Indeed, by identifying the precise nature of the defective

Fig. 8 | Targeting PI3K or MAPK pathways reverses DLV malformations. **a**, Effect of the inhibition of ERK signaling (selumetinib 1 µM) or activation of PI3K (YS-49 1 µM) or a combination of both after the development of the DLV or the malformations (72–96 hpf). Maximum projection of the DLV from *Tg(kdrl:GFP)* WT, *rasa1a*$^{+/-}$ and *ephb4a*$^{+/-}$ with a choroidal malformation before and after the pharmacological treatment on the same larvae (72 hpf and 96 hpf). Within the small white square is a transversal section at the location of the dashed line showing the vessel's structure. Quantification of the percentage of choroidal malformation before and after the treatment of *rasa1a*$^{+/-}$ larvae (DMSO, $n = 4$; selumetinib, $n = 7$; YS-49, $n = 7$; and selumetinib + YS-49, $n = 8$) and *ephb4a*$^{+/-}$ (DMSO, $n = 6$; selumetinib, $n = 5$; YS-49, $n = 9$; and selumetinib + YS-49, $n = 4$). Selu, selumetinib. **b**, Effect of the inhibition of ERK signaling (selumetinib 1 µM), activation of PI3K (YS-49 1 µM) or a combination of both (YS-49 and selumetinib) after the development of the DLV or the malformations (72–96 hpf). Maximum projection of the DLV from *Tg(kdrl:GFP)* WT, *rasa1a*$^{+/-}$ and *ephb4a*$^{+/-}$ with a mural malformation before and after the pharmacological treatment on the same larvae (72 hpf and 96 hpf). Quantification of the average diameter of the mural malformation before and after the treatment of the WT, *rasa1a*$^{+/-}$ (DMSO: $n = 16$ WT, $n = 9$ *rasa1a*$^{+/-}$; selumetinib: $n = 11$ WT, $n = 7$ *rasa1a*$^{+/-}$; YS-49: $n = 11$ WT, $n = 6$ *rasa1a*$^{+/-}$; and selumetinib + YS-49: $n = 13$ WT, n = 6 *rasa1a*$^{+/-}$) and *ephb4a*$^{+/-}$ larvae (DMSO: $n = 13$ WT, $n = 12$ *ephb4a*$^{+/-}$; selumetinib: $n = 17$ WT, $n = 10$ *ephb4a*$^{+/-}$; YS-49: $n = 7$ WT, $n = 7$ *ephb4a*$^{+/-}$; and selumetinib + YS-49: $n = 13$ WT, $n = 10$ *ephb4a*$^{+/-}$). Statistical analysis: ANOVA with Tukey's test for multiple comparisons.

https://doi.org/10.1038/s44161-025-00659-5

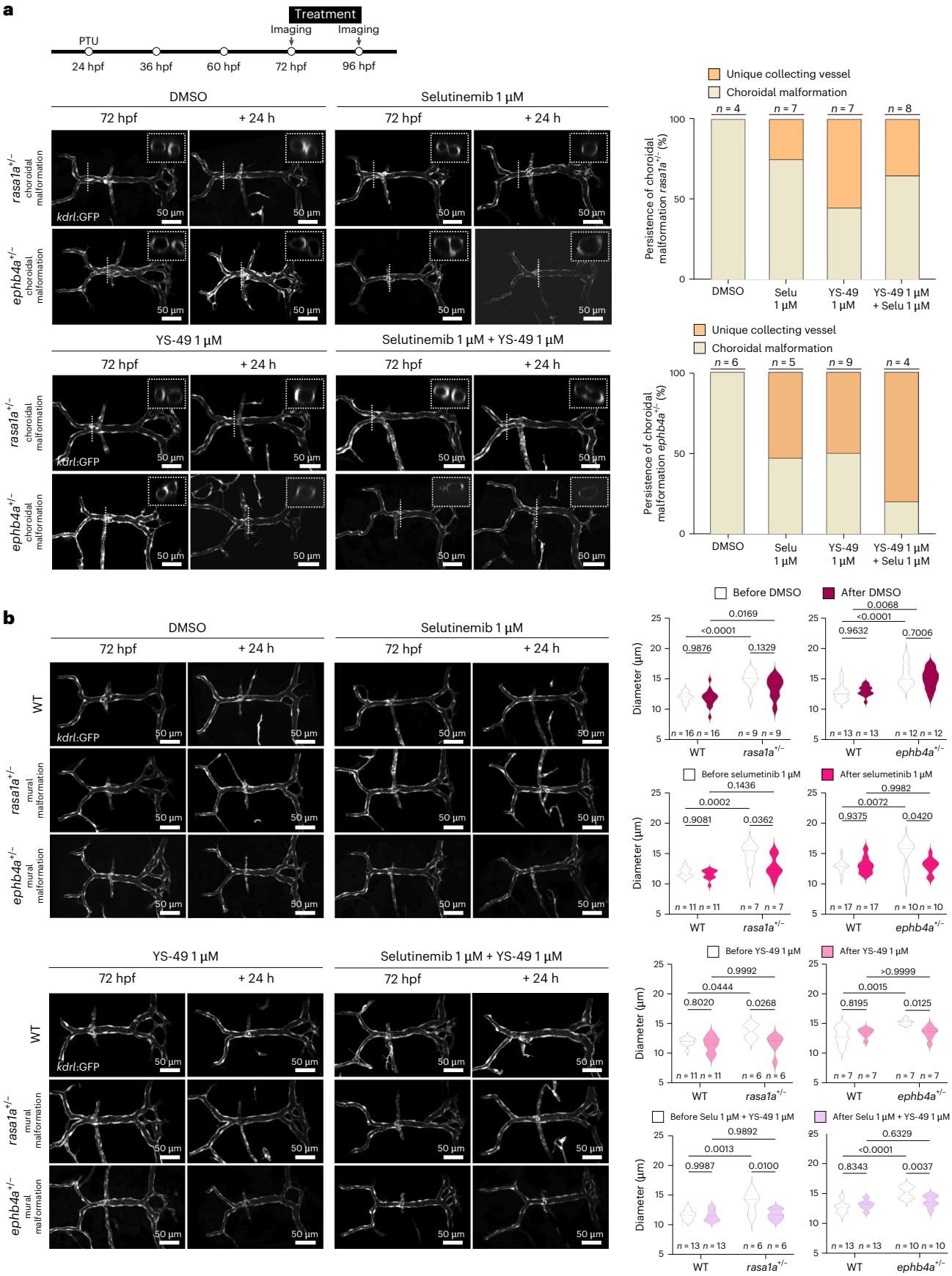

tissular mechanism leading to the malformations in a zebrafish model and by identifying specific molecular actors of flow-mediated vessel fusion, we enable the rapid development of targeted strategies not only for VGAMs but also for other types of diseases triggered by vascular remodeling.

Methods

Clinical imaging of VGAMs

Two patients who had undergone endovascular treatment for VGAM lesions in the neurointerventional unit of Erasme Hospital (Brussels, Belgium) were selected to provide representative imaging of a choroidal malformation (patient: male, neonate, premature cesarian delivery at 38 weeks of pregnancy consecutive to decompensated heart failure) or of a mural malformation (patient: male, 5 years old). Digital subtraction angiography (Philips, Allura biplane system) was performed before the endovascular intervention to provide a precise evaluation of the VGAM angioarchitecture and provide access to endovascular treatment of the lesion. This study has been approved by the Erasme Hospital ethical committee under protocol number P2022/256 'Prise en charge des anomalies cérébrales vasculaires à l'hopital Erasme'. Informed and signed consent for using these clinical images was obtained retrospectively from the patient's legal guardians.

Zebrafish husbandry

Zebrafish (*Danio rerio*) were maintained at 28 °C on a 14-h light and 10-h dark cycle. Embryos were obtained and raised under standard conditions in accordance with European and national ethical and animal welfare guidelines (protocol approval number: CEBEA-07 GOS IBMM). Mutant and transgenic lines used in this study are Tg(kdrl:GFP)s843 (ref. 56), Tg(gata1a:DsRed)sd2 (ref. 57), Tg(kdrl:rasmCherry)s896 (ref. 58), Tg(kdrl:NLS-mCherry)is4 (ref. 59), *rasa1a*^{ulb28} (generated in this study) and *ephb4a*^{hu3445} (ENU-induced point mutation obtained from the Zebrafish International Resource Center, ZFIN ID: ZDB-ALT-100723-5). The developmental stages were determined according to standard staging series[60].

Mutant generation

The *rasa1a* allele was generated using the CRISPR–Cas9 technology as described previously[61,62]. The targeting small guide RNAs were designed using the https://chopchop.cbu.uib.no website and were cloned into pT7-gRNA plasmid vector using the following primers: rasa1a-fwd: 5′-TAGGATTGCGTCAGGCTCGGACAC-3′ and rasa1a-rv: 5′-AAACGTGTCCGAGCCTGACGCAAT-3′. The small guide RNA was transcribed from the BamHI-linearized pT7-gRNA vector using the MEGAshortscript T7 transcription kit (Thermo Fisher Scientific) and injected at 50 pg into one-cell-stage zebrafish embryos, together with 150 pg of *nls–zCas9–nls* mRNA transcribed from the *pT3TS–zCas9–nls* vector (Addgene number 46757) using the mMessage mMachine T3 Kit (Ambion). The efficiency of somatic gene disruption was assessed using high-resolution melt analysis on the Illumina Eco Real-Time PCR system and further validated by Sanger sequencing.

Morpholino injection and microangiography

A total of 0.25 ng of the *tnnt2a* morpholino (CATGTTTGCTCTGATC TGACACGCA, GeneTools), 1 ng of the *rasa1a* morpholino (TAATCTCCAC ACATCGCAATGATCC, GeneTools), 0.5 ng of *ephb4a* (CTGGAAAA CACACACGAGAGATAGA, GeneTools) and 2 ng of a standard control morpholino (CCTCTTACCTCAGTTACAATTTATA, GeneTools) were injected into one-cell-stage embryos. To assess DLV perfusion, microangiography was conducted by injecting 1 nl of 10 kDa cascade blue (10 mg ml^{-1}) into the bloodstream through the duct of Cuvier of anesthetized 36-hpf embryos using a micromanipulator. Embryos were mounted dorsally and imaged individually 30 min postinjection to capture tracer distribution in the vascular network.

Rescue experiments were performed as follows: zebrafish RNA was extracted from 20 embryos of 30-hpf zebrafish using an EZ-10 DNAaway RNA Miniprep Kit (Bio Basic, catalog number BS88136) according to the manufacturer's protocol. cDNA was subsequently synthetized using the Superscript III First Strand Synthesis System (Invitrogen, catalog number 18080051) according to the manufacturer's protocol, and the *rasa1a* coding sequence was amplified using the following primers: 5′-ATGGAGGTGAGGGGCGAGGACAGG-3′ and 5′-CTACCTGCTGCTGTTGGACATGGC-3′ using Phusion High Fidelity DNA Polymerase (New England Biolabs, catalog number M0530L). The *rasa1a* cds was then cloned into the pCS2+ backbone for mRNA production and injection and pminiTol2 backbone for injection and Tol2-transposase-mediated transgenesis. *Rasa1a* mRNA was produced using the mMESSAGE mMACHINE SP6 Transcription Kit (Invitrogen, catalog number AM1340) and injected at a concentration of 100 ng in one-cell-stage zebrafish embryos. The *pminiTol2_fli1:rasa1a-p2A-mKate* vector was injected at a concentration of 15 pg, and *transposase* mRNA was co-injected at a concentration of 25 pg in one-cell-stage zebrafish embryos. Half of the injected embryos were then subsequently injected with a morpholino against *tnnt2a* at a concentration of 0.25 ng in the one-cell-stage zebrafish embryos. Embryos were raised under standard conditions and treated with 0.003% propylthiouracile (PTU) after 24 h. At 72 hpf, larvae were anesthetized with tricaine and immobilized in 1% low-melting-point agarose in a glass-bottom Petri dish (MatTek) before imaging using a Zeiss LSM 900 confocal microscope with a ×20 objective. All experiments were replicated three times.

Phenotyping

Phenotypic analysis of *ephb4a* morpholino (MO), *rasa1a* MO and control larvae was conducted at 3 dpf using a Leica M165 stereoscope to identify morphological abnormalities, including cardiac and cerebral edema. For *ephb4a* MO larvae, Z-stack imaging of the DLV was conducted using a spinning-disk confocal microscope (Yokogawa CSU-X1 on a Zeiss inverted stand) with a ×20/0.5 Plan Apo objective and Metamorph software. Imaging of *rasa1a* MO was performed using a Zeiss LSM710 confocal microscope with a ×20/0.8 dry objective and driven by Zen Blue software. For mutants and WT larvae, general vasculature imaging was obtained using a Nikon AX R confocal microscope equipped with a ×25/1.05 Plan Apo Lambda S silicone objective. Large field-of-view images (3 × 1) were acquired using a ×10/0.45 Plan Apo Lambda D lens and analyzed using NIS software. Cardiac edema and ISV defects—characterized by vessel duplication or absence of perfusion—were quantified from large Z-stack acquisitions obtained using the ×10 objective on the Nikon AX R or a Leica stereoscope. Characterization of choroidal and mural malformations was performed using Z-stack acquisitions with the same Nikon AX R confocal microscope equipped with a ×25 silicone immersion objective. Choroidal malformations were described as two dissociated perfused vessels on the anterior segment with or without two or three distinctive vessels on the posterior segment. Mural malformations were characterized by vessel dilatation in the posterior segment.

Cardiac function in zebrafish

Ventricular and atrial volumes were determined via video recordings captured using the Nikon AX confocal microscope (Nikon Instruments). Imaging was performed using the ×25/1.05 Plan Apo Lambda S silicone immersion objective at an average acquisition speed of 10 frames per second. These data were calculated by extracting measurements of long-axis (lax) and short-axis (sax) ventricular and atrial diameters from static images obtained at the end of systole, showing maximal dilation, and the end of diastole. NIS software was used to carry out these measurements, which were then used in equation (1) to determine both atrial and ventricular volumes.

$$V = 0.5 \times \mathrm{sax}^2 \times \mathrm{lax} \quad (1)$$

To determine the stroke volume, we computed it by subtracting the average diastolic ventricular volume from the average systolic ventricular volume.

Imaging and hemodynamic parameter analysis

Embryos were imaged using a Nikon AX R confocal microscope (Nikon Instruments) using ×10, ×20 and ×25 silicon immersion objectives, Nikon spinning-disk microscope using a ×40 immersion objective, spinning-disk confocal microscope (Yokogawa CSU-X1 on a Zeiss inverted stand) using a ×20/0.5 Plan Apo objective and Leica M165 stereoscope. The live imaging experiments could be done after the embryos or larvae were anesthetized with tricaine (19.2 mg l^{-1}, Sigma-Aldrich), dechorionated and immobilized in 1% low-melting-point agarose in a glass-bottom Petri dish (MatTek). After the imaging, the embryos were genotyped using high-resolution melt analysis (Eco Illumina real-time PCR system). Images of the DLV embryos were acquired with the Nikon AX R with a ×25 objective; specifically, the large image (3 × 1) of embryos was acquired with a ×10 objective. The living zebrafish embryos were immobilized in 1% low-melting-point agarose E3 medium (0.3 g l^{-1} Instant Ocean salt, 75 mg l^{-1} $CaSO_4$, 1 mg l^{-1} methylene blue) supplemented with *N*-phenylthiourea (30 mg l^{-1}, Sigma-Aldrich) and tricaine (19.2 mg l^{-1}, Sigma-Aldrich). For the time-lapse analysis, we used two approaches: the Nikon AX R confocal microscope with a stable temperature of 28.5 °C was maintained using a heating chamber, and the X-Light V3 spinning-disk confocal microscope (CrestOptics) with an NiR Apo ×40/0.80 DIC N2 water immersion objective, specifically for the overdose of tricaine experiment (×4). Assembly of confocal stacks and time-lapse videos was conducted using NIS software. Blood flow measurement was performed by rapidly tracking erythrocyte movement using the transgenic line *Tg(kdrl:GFP;gata1a:DsRed)*. For the frequency profile (Fig. 3), we used a spinning-disk confocal microscope (Yokogawa CSU-X1 on a Zeiss inverted stand) equipped with a sensitive and ultra-fast electron-multiplying charge-coupled device camera (Photometrics Evolve 512) and a ×20/0.5 Plan Apo Lambda D objective. For each sample, the displacement of erythrocytes required an acquisition speed of 200 frames per second with 3,000 frames. This acquisition speed allows automated analysis of the velocities by tracking the erythrocytes individually, image by image, via the scientific imaging software Fiji and the image analysis module TrackMate v.7 (ref. 63). This software allows both obtaining a plot of the instantaneous velocities of erythrocytes and calculating the average velocity by integrating the velocity peaks. For the calculation of the fundamental frequency, the frequency profile (Fig. 2) and blood parameters (Extended Data Fig. 2), we used a spinning-disk confocal microscope (X-Light V3, CrestOptics) equipped with a fast camera (Prime BSI Scientific CMOS (sCMOS)) with an acquisition speed of 750 frames per second and an NiR Apo ×40/0,80 DIC N2 water immersion objective. The fundamental frequency of the red blood cells' velocity was programmatically assessed using MATLAB version R2021b. Velocity and time data generated by TrackMate v.7 were imported as vectors. The sampling frequency was calculated as the inverse of the average time step between each point of the time vector. Subsequently, a frequency vector was computed as shown in equation (2), following the Nyquist–Shannon sampling theorem with fs being the sampling frequency and *n* the sampling rate.

$$f = (0 : n - 1)(\mathrm{fs}/n) \tag{2}$$

The discrete Fourier transform of the velocity vector was then computed using the fast Fourier transform function. The findpeaks function was applied to the fast Fourier transform spectrum to identify the peak corresponding to the fundamental frequency. Finally, the peak position was used to determine the value of the fundamental frequency.

The average diameter measurements were performed on a maximum stack projection. We manually analyzed the vessel diameter at three different points along its length via NIS software. The data set of average globule velocities and the mean diameter of each vessel allowed us to estimate the shear stress. Shear stress (τi) was estimated by measuring the average diameter of the blood vessel and the mean velocity of red blood cells as an approximation of the debit; we did not consider the non-Newtonian nature of blood at this scale, but the blood vessels in zebrafish embryos have roughly similar dimensions in the micrometer range. We used equation (3) to estimate it.

$$\tau i = 4\eta Qi/\pi Ri^3 \tag{3}$$

where η is the blood viscosity, Qi is the average velocity (μm s^{-1}) and Ri is the vessel diameter (μm). To show the generation of two independent streams, the tracks of red blood cells produced by TrackMate were sorted using a Python program (Jupyter Notebook version 6.4.5 running using Conda 4.14.0 and Python 3). For each track, the initial and final positions of the red blood cells were identified with respect to the *x* and *y* axes. A central axis was then created to follow the direction of the DLV. Tracks were then sorted based on the position of their initial and final points relative to the central axis. Tracks were then assigned different colors based on this sorting.

Immunolabeling-enabled three-dimensional imaging of solvent-cleared organs protocol for tissue clearing and volumetric imaging

The described method was adapted from the immunolabeling-enabled three-dimensional imaging of solvent-cleared organs protocol[64]. Mice were purchased from Charles River, transported and maintained in a certified animal facility in accordance with European guidelines. The room temperature ranged from 20 °C to 25 °C. The relative ambient humidity at the level of the mouse cages was 55 ± 15%. Each cage was provided with food, water and two types of nesting material. A semi-natural light cycle of 12 h–12 h light–dark was used. Postmortem tissue collection was approved by the Ethical Committee for Animal Welfare (Commission d'Ethique et du Bien Etre Animal (CEBEA), Faculty of Medicine, Université Libre de Bruxelles, protocol 745N). Tissues collected were fixed overnight at 4 °C in 4% PFA diluted in PBS. After fixation, the samples were washed three times for 1 h each in PBS and subsequently dehydrated using a series of methanol–PBS solutions (50%, 80%, 100%, 100%) for 1 h at room temperature. The samples were then bleached in 5% H_2O_2 in 20% DMSO–methanol overnight at 4 °C. After bleaching, the samples were washed in 100% methanol for 1 h twice, then in 20% DMSO–methanol for 2 h, then in 80% methanol for 1 h, 50% methanol for 1 h, PBS for 1 h twice, and finally in PBS–0.2% Triton X-100 for 1 h twice before staining. Pretreated samples were incubated in PBS–2% Triton X-100–20% DMSO–0.3 M glycine at 37 °C overnight. The samples were blocked in 2% Triton X-100–Intercept (PBS) Blocking Buffer (LI-COR) at 37 °C for 2 days and then were washed twice for 1 h each in PBS containing 0.1% Tween-20. Subsequently, the samples were incubated with the primary antibody PECAM-1 (R&D AF3628 at a dilution of 1:500) in 2% Triton Blocking Buffer at 37 °C for 4 days. After the incubation, the samples were washed with PBS containing 0.1% Tween-20 at various time intervals (10 min, 15 min, 30 min, 1 h, 2 h and overnight). Next, the samples were incubated with a secondary antibody (donkey anti-goat IgG (H+L) highly cross-adsorbed secondary antibody, Alexa Fluor Plus 555 from Thermo Fisher, reference A32816, at a dilution of 1:1,000 in 2% Triton Blocking Buffer) at 37 °C for 4 days. Further washes were performed using PBS with 0.1% Tween-20 at various time intervals (10 min, 15 min, 30 min, 1 h, 2 h and 1 day). Immunolabeled tissues were then incubated overnight in a solution of 50% tetrahydrofuran–H_2O, followed by incubation in 80% tetrahydrofuran for 1 h and 100% tetrahydrofuran for 2 h. Subsequently, the samples were incubated in dichloromethane until they sank to the bottom of the vial. Finally, the samples were cleared and stored in dibenzyl ether. The tissues were fixed on glass-bottom dishes and imaged using a Nikon AX confocal microscope with a ×25/1.05 Plan Apo Lambda S silicone objective.

Cell culture

HUVECs were purchased from Lonza (number C2519A) and cultured on gelatin-coated tissue culture dishes with EGM-2 culture medium (Lonza). Cells were used between passages 3 and 5 for the experiments. siRNA transfection was performed with Lipofectamine RNAiMax and ONTarget siRNA (Horizon Discovery Bioscience), reference L-005276-00-0005 for Rasa1 and D-001810-10-05 for the non-targeting scramble siRNA. VEGF 50 ng ml^{-1} (Thermo Fisher) was used as a chemical agonist. Shear stress application, western blot experiment and immunostaining of HUVECs were previously described[5]. Briefly, cells were seeded on fibronectin-coated slides (20 µg ml^{-1}) and grown to confluence. For short-term experiments (up to 30 min), cells were starved in EBM-2 medium with 0.2% FBS for 4 h. For long-term experiments (more than 4 h), cells were starved for 1 h in 0.2% FBS–EBM. Shear stress of 12 dyn cm^{-2} was applied in a parallel-flow chamber for the indicated times. Cells were fixed with 4% PFA, permeabilized with 1% Triton X-100, blocked and incubated for 1 h with phalloidin (Alexa Fluor Plus 647 Phalloidin from Invitrogen, reference A30107, at a dilution of 1/1,000) and DAPI (from Invitrogen, reference 62248, at a dilution of 1/1,000) at room temperature. For western blots, cells were washed with cold PBS and lysed in SL-DOC buffer, and proteins were separated via SDS–BOLT 4–12% Bis–Tris gels, transferred to nitrocellulose membranes, blocked with blocking buffer and probed with primary antibodies against pERK1/2 (Phospho-ERK1/2 (Thr202/Tyr204) from Proteintech, reference 28733-1, at a 1:2,000 dilution), pAKT ser473 (Phospho-Akt (Ser473) from Cell Signaling, reference 4060, at a 1:2,000 dilution), RASA1 (rasa1 B4F8 clone from Invitrogen, reference MA4-001, at a 1:2,000 dilution) and actin (β-Actin from Sigma, reference A5441, at a 1:2,000 dilution), followed by detection with DyLight PEG-conjugated secondary antibodies (from Cell Signaling: anti-mouse IgG (H+L) (DyLight 680 Conjugate), reference 5470, and anti-rabbit IgG (H+L) (DyLight 800 4X PEG Conjugate), reference 5151, both at a 1:20,000 dilution).

Construction of a millifluidic flow chamber

The chamber model was designed on Solidworks. It was then three-dimensionally printed using a Formlabs 3D Printer with Dental SG material. After printing, the chamber was filled with SYLGARD 184 Silicone and incubated at 65 °C overnight to solidify. On the second day, the silicone model was carefully released from the chamber. The chamber was assembled with a glass slide coated with fibronectin and HUVECs. The flow was introduced into the model through two inputs and one output using microtubes connected to an Elveflow microfluidics pump OB1 (Elvesys), generating separate flows for each inlet with controlled pressure. Flow meters were used to control debit right before the inlet. For our experiments, we used a phase shift of 180° for the pressure wave between each inlet. The micro fluorescence beads diluted in water (FluoSpheres Polystyrene Microspheres, 1.0 µm, blue-green (430/465)) were perfused into the left channel, and the right channel was perfused with pure water. Images were obtained through a fast time-lapse recording using a spinning-disk microscope (X-Light V3, CrestOptics) equipped with a fast camera (Prime BSI sCMOS) and a Plan Apo ×20/0.75 DIC N2 objective.

Intracellular calcium imaging

HUVECs (Lonza) obtained commercially were used between passages 4 and 5 and cultured using EGM-2 medium. The cells were seeded onto glass coverslips coated with fibronectin at a concentration of 20 µg ml^{-1}. Once the cells reached confluency, they were incubated with a calcium dye working solution in an incubator at 37 °C for 40 min. The calcium dye working solution was prepared by mixing Calbryte-520 AM (AAT Bioquest) with 4% FBS–EBM to achieve a final concentration of 5 µM. In addition, 0.04% Pluronic F-127 was included in the solution. Before imaging, the medium was changed to 2% FBS–EBM at room temperature for 10 min. Coverslips containing cells were embedded in the microfluidics chamber and perfused with 2% FBS–EBM. We captured images within the collecting channel at intervals of 2 s for 30 min using a spinning-disk microscope (X-Light V3, CrestOptics) equipped with a fast camera (Prime BSI sCMOS) and a Plan Apo ×20/0.75 DIC N2 objective.

Pharmacological treatment of *rasa1a* and *ephb4a* mutants

We performed two different protocols to study the imbalance in flow activation of PI3K/ERK signaling. In the first protocol, dechorionated embryos were incubated from 36 hpf to 60 hpf (time of the beginning of the formation of the DLV) and from 60 hpf to 72 hpf in E3 medium (0.3 g l^{-1} Instant Ocean salt, 75 mg l^{-1} $CaSO_4$, 1 mg l^{-1} methylene blue) supplemented with PTU (30 mg l^{-1}, Sigma-Aldrich); the different drugs DMSO (Sigma-Aldrich), 1 µM selumetinib (TOCRIS) and 1 µM YS-49 (MCE); and a combination of selumetinib and YS-49. Embryos were anesthetized with tricaine (19.2 mg l^{-1}, Sigma-Aldrich) immobilized in 1% low-melting-point agarose in a glass-bottom Petri dish (MatTek), mounted dorsally and individually imaged using a Nikon AX confocal microscope with a ×25 silicon immersion objective. In the second protocol, dechorionated embryos were anesthetized, immobilized, mounted dorsally and imaged with the ×25 objective at 72 hpf. Embryos were taken away from the glass-bottom Petri dish and incubated from 72 hpf to 96 hpf (after the complete development of the DLV) in E3 medium supplemented with PTU and the same drugs previously described. After anesthesia, the embryos were remounted to image the DLV after drug treatment with the same imaging parameters. For the two protocols, after the imaging (at 72 hpf for the first one and 96 hpf for the second), the embryos were genotyped using high-resolution melt analysis (Eco Illumina real-time PCR system).

List of antibodies and labeling reagents

All antibodies and labeling reagents are presented in Supplementary Table 1.

Statistics and reproducibility

Statistical analysis was performed using the GraphPad Prism 10 software (v.10.4.1). Data are expressed as mean ± s.e.m., and the distribution is shown within the graphs. Two-tailed *P* values were calculated by various tests, depending on the normality of the data distribution in GraphPad Prism, as indicated in the figure legends. All experiments involving micrographs or videos were observed at least three times on independent samples.

Reporting summary

Further information on research design is available in the Nature Portfolio Reporting Summary linked to this article.

Data availability

The data that support the findings of this study are available in the Article and Supplementary Information.

References

1. Franco, C. A. et al. Dynamic endothelial cell rearrangements drive developmental vessel regression. *PLoS Biol.* **13**, e1002125 (2015).
2. Djonov, V., Baum, O. & Burri, P. H. Vascular remodeling by intussusceptive angiogenesis. *Cell Tissue Res.* **314**, 107–117 (2003).
3. Chouinard-Pelletier, G., Jahnsen, E. D. & Jones, E. A. Increased shear stress inhibits angiogenesis in veins and not arteries during vascular development. *Angiogenesis* **16**, 71–83 (2013).
4. Baeyens, N., Bandyopadhyay, C., Coon, B. G., Yun, S. & Schwartz, M. A. Endothelial fluid shear stress sensing in vascular health and disease. *J. Clin. Invest.* **126**, 821–828 (2016).
5. Baeyens, N. et al. Defective fluid shear stress mechanotransduction mediates hereditary hemorrhagic telangiectasia. *J. Cell Biol.* **214**, 807–816 (2016).

6. Baeyens, N. et al. Vascular remodeling is governed by a VEGFR3-dependent fluid shear stress set point. *eLife* https://doi.org/10.7554/eLife.04645 (2015).
7. Baeyens, N. & Schwartz, M. A. Biomechanics of vascular mechanosensation and remodeling. *Mol. Biol. Cell.* **27**, 7–11 (2016).
8. Lv, X., Jiang, C. & Wang, J. Pediatric intracranial arteriovenous shunts: advances in diagnosis and treatment. *Eur. J. Paediatr. Neurol.* **25**, 29–39 (2020).
9. Queisser, A., Seront, E., Boon, L. M. & Vikkula, M. Genetic basis and therapies for vascular anomalies. *Circ. Res.* **129**, 155–173 (2021).
10. Duran, D. et al. Human genetics and molecular mechanisms of vein of Galen malformation. *J. Neurosurg. Pediatr.* **21**, 367–374 (2018).
11. Eerola, I. et al. Capillary malformation–arteriovenous malformation, a new clinical and genetic disorder caused by *RASA1* mutations. *Am. J. Hum. Genet.* **73**, 1240–1249 (2003).
12. Revencu, N. et al. Parkes Weber syndrome, vein of Galen aneurysmal malformation, and other fast-flow vascular anomalies are caused by *RASA1* mutations. *Hum. Mutat.* **29**, 959–965 (2008).
13. Revencu, N. et al. *RASA1* mosaic mutations in patients with capillary malformation–arteriovenous malformation. *J. Med. Genet.* **57**, 48–52 (2020).
14. Lubicz, B. & Christiaens, F. Endovascular treatment of intracranial vascular malformations in children. *Dev. Med. Child Neurol.* **62**, 1124–1130 (2020).
15. Yan, J., Wen, J., Gopaul, R., Zhang, C. Y. & Xiao, S. W. Outcome and complications of endovascular embolization for vein of Galen malformations: a systematic review and meta-analysis. *J. Neurosurg.* **123**, 872–890 (2015).
16. Jaimes, C. et al. Brain injury in fetuses with vein of Galen malformation and nongalenic arteriovenous fistulas: static snapshot or a portent of more? *AJNR Am. J. Neuroradiol.* **43**, 1036–1041 (2022).
17. Kawasaki, J. et al. RASA1 functions in EPHB4 signaling pathway to suppress endothelial mTORC1 activity. *J. Clin. Invest.* **124**, 2774–2784 (2014).
18. Vivanti, A. et al. Loss of function mutations in EPHB4 are responsible for vein of Galen aneurysmal malformation. *Brain* **141**, 979–988 (2018).
19. Taffin, H. et al. Long-term outcome of vein of Galen malformation. *Dev. Med. Child Neurol.* **62**, 729–734 (2020).
20. Amyere, M. et al. Germline loss-of-function mutations in EPHB4 cause a second form of capillary malformation–arteriovenous malformation (CM-AVM2) deregulating RAS-MAPK signaling. *Circulation* **136**, 1037–1048 (2017).
21. Komiyama, M. The median vein of prosencephalon of Markowski: from morphology to genetics. *Interv. Neuroradiol.* **26**, 752–756 (2020).
22. Aurboonyawat, T., Suthipongchai, S., Pereira, V., Ozanne, A. & Lasjaunias, P. Patterns of cranial venous system from the comparative anatomy in vertebrates. Part I, introduction and the dorsal venous system. *Interv. Neuroradiol.* **13**, 335–344 (2007).
23. Buratti, S. et al. Vein of Galen aneurysmal malformation in newborns: a retrospective study to describe a paradigm of treatment and identify risk factors of adverse outcome in a referral center. *Front. Pediatr.* **11**, 1193738 (2023).
24. Sehnert, A. J. et al. Cardiac troponin T is essential in sarcomere assembly and cardiac contractility. *Nat. Genet.* **31**, 106–110 (2002).
25. Kugler, E. et al. The effect of absent blood flow on the zebrafish cerebral and trunk vasculature. *Vasc. Biol.* **3**, 1–16 (2021).
26. Goumans, M. J., Zwijsen, A., Ten Dijke, P. & Bailly, S. Bone morphogenetic proteins in vascular homeostasis and disease. *Cold Spring Harb. Perspect. Biol.* https://doi.org/10.1101/cshperspect.a031989 (2018).
27. Eker, O. F. et al. European Reference Network for Rare Vascular Diseases (VASCERN) position statement on cerebral screening in adults and children with hereditary haemorrhagic telangiectasia (HHT). *Orphanet J. Rare Dis.* **15**, 165 (2020).
28. Orme, C. M., Boyden, L. M., Choate, K. A., Antaya, R. J. & King, B. A. Capillary malformation–arteriovenous malformation syndrome: review of the literature, proposed diagnostic criteria, and recommendations for management. *Pediatr. Dermatol.* **30**, 409–415 (2013).
29. Ngo, I. L. et al. A study on mixing performance of dean flows through spiral micro-channel under various effects. *Phys. Fluids* https://doi.org/10.1063/1.5142884 (2020).
30. Lee, C. Y., Chang, C. L., Wang, Y. N. & Fu, L. M. Microfluidic mixing: a review. *Int. J. Mol. Sci.* **12**, 3263–3287 (2011).
31. Baeyens, N. Fluid shear stress sensing in vascular homeostasis and remodeling: towards the development of innovative pharmacological approaches to treat vascular dysfunction. *Biochem. Pharmacol.* **158**, 185–191 (2018).
32. Baeyens, N. et al. Syndecan 4 is required for endothelial alignment in flow and atheroprotective signaling. *Proc. Natl Acad. Sci. USA* **111**, 17308–17313 (2014).
33. Pamonsinlapatham, P. et al. p120-Ras GTPase activating protein (RasGAP): a multi-interacting protein in downstream signaling. *Biochimie* **91**, 320–328 (2009).
34. Song, M. & Finley, S. D. ERK and Akt exhibit distinct signaling responses following stimulation by pro-angiogenic factors. *Cell Commun. Signal.* **18**, 114 (2020).
35. Yeh, T. C. et al. Biological characterization of ARRY-142886 (AZD6244), a potent, highly selective mitogen-activated protein kinase kinase 1/2 inhibitor. *Clin. Cancer Res.* **13**, 1576–1583 (2007).
36. Hsu, Y. H., Chang, C. C., Yang, N. J., Lee, Y. H. & Juan, S. H. RhoA-mediated inhibition of vascular endothelial cell mobility: positive feedback through reduced cytosolic p21 and p27. *J. Cell. Physiol.* **229**, 1455–1465 (2014).
37. Gebala, V., Collins, R., Geudens, I., Phng, L. K. & Gerhardt, H. Blood flow drives lumen formation by inverse membrane blebbing during angiogenesis in vivo. *Nat. Cell Biol.* **18**, 443–450 (2016).
38. Daems, M., Peacock, H. M. & Jones, E. A. V. Fluid flow as a driver of embryonic morphogenesis. *Development* https://doi.org/10.1242/dev.185579 (2020).
39. Chen, Q. et al. Haemodynamics-driven developmental pruning of brain vasculature in zebrafish. *PLoS Biol.* **10**, e1001374 (2012).
40. Arpino, J. M. et al. Low-flow intussusception and metastable VEGFR2 signaling launch angiogenesis in ischemic muscle. *Sci. Adv.* **7**, eabg9509 (2021).
41. Simpson, L. J. & Tzima, E. To fuse or not to fuse. *Arterioscler. Thromb. Vasc. Biol.* **38**, 1959–1960 (2018).
42. Caolo, V. et al. Shear stress and VE-cadherin. *Arterioscler. Thromb. Vasc. Biol.* **38**, 2174–2183 (2018).
43. Tzima, E. et al. A mechanosensory complex that mediates the endothelial cell response to fluid shear stress. *Nature* **437**, 426–431 (2005).
44. Orsenigo, F. et al. Phosphorylation of VE-cadherin is modulated by haemodynamic forces and contributes to the regulation of vascular permeability in vivo. *Nat. Commun.* **3**, 1208 (2012).
45. Henkemeyer, M. et al. Vascular system defects and neuronal apoptosis in mice lacking ras GTPase-activating protein. *Nature* **377**, 695–701 (1995).

46. Lubeck, B. A. et al. Blood vascular abnormalities in Rasa1(R780Q) knockin mice: implications for the pathogenesis of capillary malformation–arteriovenous malformation. *Am. J. Pathol.* **184**, 3163–3169 (2014).
47. Greysson-Wong, J. et al. *rasa1*-related arteriovenous malformation is driven by aberrant venous signalling. *Development* https://doi.org/10.1242/dev.201820 (2023).
48. Chen, D., Teng, J. M., North, P. E., Lapinski, P. E. & King, P. D. RASA1-dependent cellular export of collagen IV controls blood and lymphatic vascular development. *J. Clin. Invest.* **129**, 3545–3561 (2019).
49. Zhou, J., Li, Y. S. & Chien, S. Shear stress-initiated signaling and its regulation of endothelial function. *Arterioscler. Thromb. Vasc. Biol.* **34**, 2191–2198 (2014).
50. Sugden, W. W. et al. Endoglin controls blood vessel diameter through endothelial cell shape changes in response to haemodynamic cues. *Nat. Cell Biol.* **19**, 653–665 (2017).
51. Jin, Y. et al. Endoglin prevents vascular malformation by regulating flow-induced cell migration and specification through VEGFR2 signalling. *Nat. Cell Biol.* **19**, 639–652 (2017).
52. Deng, H. et al. Activation of Smad2/3 signaling by low fluid shear stress mediates artery inward remodeling. *Proc. Natl Acad. Sci. USA* https://doi.org/10.1073/pnas.2105339118 (2021).
53. Tiezzi, M., Deng, H. & Baeyens, N. Endothelial mechanosensing: a forgotten target to treat vascular remodeling in hypertension? *Biochem. Pharmacol.* **206**, 115290 (2022).
54. Luxan, G. et al. Endothelial EphB4 maintains vascular integrity and transport function in adult heart. *eLife* https://doi.org/10.7554/eLife.45863 (2019).
55. Prothero, J. & Burton, A. C. The physics of blood flow in capillaries. I. The nature of the motion. *Biophys. J.* **1**, 565–579 (1961).
56. Jin, S. W., Beis, D., Mitchell, T., Chen, J. N. & Stainier, D. Y. Cellular and molecular analyses of vascular tube and lumen formation in zebrafish. *Development* **132**, 5199–5209 (2005).
57. Traver, D. et al. Transplantation and in vivo imaging of multilineage engraftment in zebrafish bloodless mutants. *Nat. Immunol.* **4**, 1238–1246 (2003).
58. Chi, N. C. et al. Foxn4 directly regulates tbx2b expression and atrioventricular canal formation. *Genes Dev.* **22**, 734–739 (2008).
59. Wang, Y. et al. Moesin1 and Ve-cadherin are required in endothelial cells during in vivo tubulogenesis. *Development* **137**, 3119–3128 (2010).
60. Kimmel, C. B., Ballard, W. W., Kimmel, S. R., Ullmann, B. & Schilling, T. F. Stages of embryonic development of the zebrafish. *Dev. Dyn.* **203**, 253–310 (1995).
61. Jao, L. E., Wente, S. R. & Chen, W. Efficient multiplex biallelic zebrafish genome editing using a CRISPR nuclease system. *Proc. Natl Acad. Sci. USA* **110**, 13904–13909 (2013).
62. Schevenels, G. et al. A brain-specific angiogenic mechanism enabled by tip cell specialization. *Nature* **628**, 863–871 (2024).
63. Tinevez, J. Y. et al. TrackMate: an open and extensible platform for single-particle tracking. *Methods* **115**, 80–90 (2017).
64. Renier, N. et al. iDISCO: a simple, rapid method to immunolabel large tissue samples for volume imaging. *Cell* **159**, 896–910 (2014).

Acknowledgements

We thank S. Costagliola and V. Wittamer (IRIBHM, Université Libre de Bruxelles) for their guidance throughout the project and for the use of their zebrafish husbandry facility. We would also like to thank D. Rodriguez (RMIT, Australia) for his help in analyzing the properties of blood flow in zebrafish. This study was funded by the following grants: FNRS MIS F.4501.19 to N.B., ARC Consolidator to N.B., Fonds Erasme 'Etude des malformations aneurysmales de la veine de Galien' to B.L. and N.B., Fondation ULB to N.B. and ERC CoG (Ctrl-BBB 865176) to B.V.

Author contributions

E.M.-V. and Y.D. contributed equally to this work. N.B. designed the project. E.M.-V., Y.D., M. America and M. Adam performed the experiments. E.M.-V., Y.D., C.G., M. America., E.Z., B.S., M.V., B.L., B.V. and N.B. performed data analysis and/or interpreted the data. B.L., B.V. and N.B. wrote the paper, with all authors providing feedback.

Competing interests

The authors declare no competing interests.

Additional information

Extended data is available for this paper at https://doi.org/10.1038/s44161-025-00659-5.

Supplementary information The online version contains supplementary material available at https://doi.org/10.1038/s44161-025-00659-5.

Correspondence and requests for materials should be addressed to Nicolas Baeyens.

Peer review information *Nature Cardiovascular Research* thanks Kristopher Kahle and the other, anonymous, reviewer(s) for their contribution to the peer review of this work.

https://doi.org/10.1038/s44161-025-00659-5

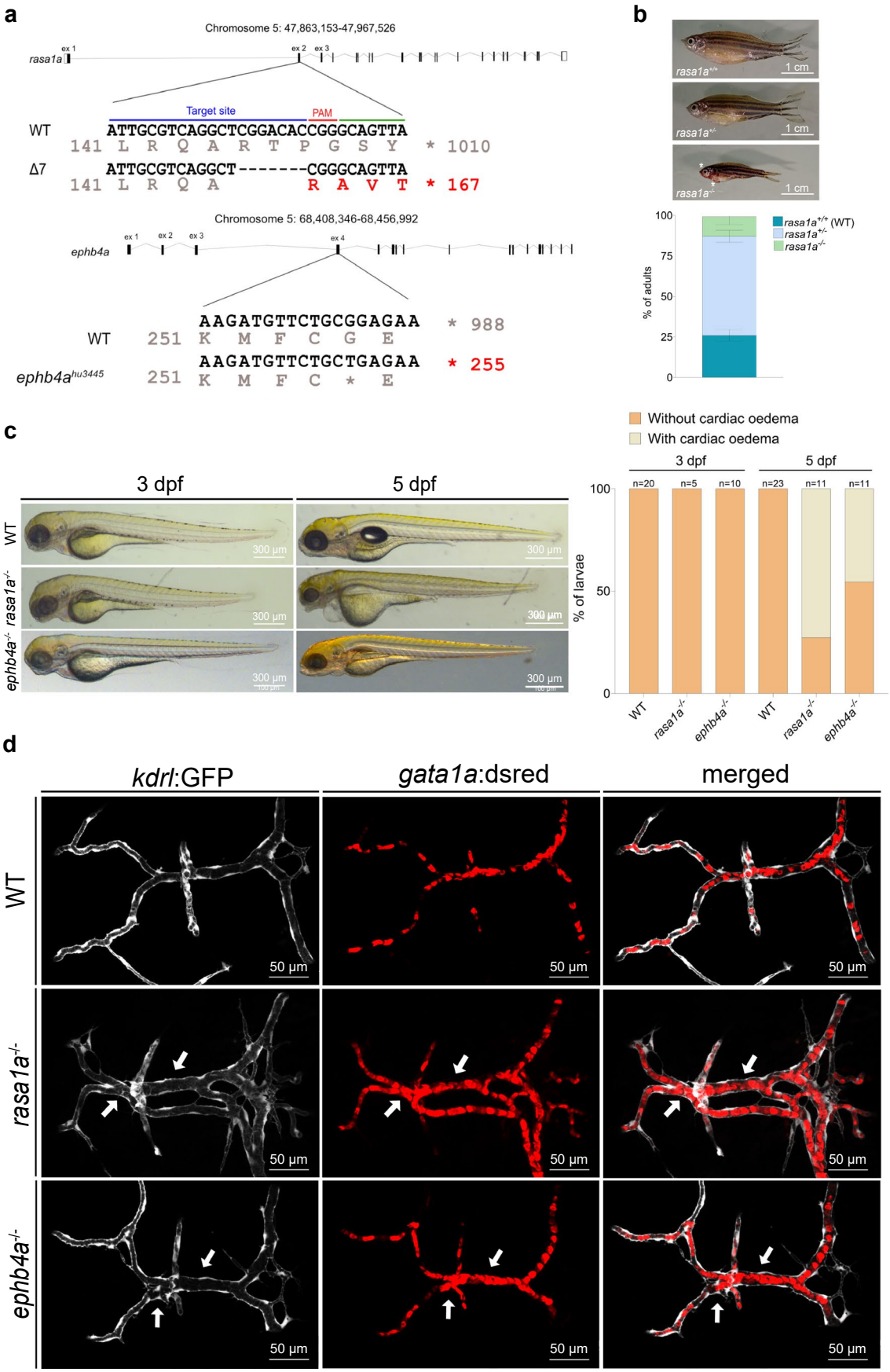

Extended Data Fig. 1 | See next page for caption.

https://doi.org/10.1038/s44161-025-00659-5

Extended Data Fig. 1 | Generation of *rasa1a* and *ephb4a* heterozygous and homozygous mutants. a. Characterization of the *rasa1a*- and *ephb4a* mutant alleles. PAM, protospacer adjacent motif. For *rasa1a*, The CRISPR/Cas9 target site is located in exon 2 of *rasa1a*. The mutant allele harbors a deletion of 7 nucleotides resulting in an early stop codon. For *ephb4a*, a single point mutation is located in exon 4 of *ephb4a* and induces a stop codon. **b**. Lateral views of the adult WT and *rasa1a* mutants (asterisk on hemorrhagic spots). Genotyping of adult zebrafish derived from 4 different *rasa1a*$^{+/-}$ incrosses (mean +/- SEM) **c**. Lateral views of WT, *rasa1a*$^{-/-}$ and *ephb4a*$^{-/-}$ larvae at 3 dpf or 5 dpf. Quantification of cardiac edema in WT, *rasa1a*$^{-/-}$ and *ephb4a*$^{-/-}$ larvae at 3 dpf (n = 20 WT, n = 5 *rasa1a*$^{-/-}$ and n = 10 *ephb4a*$^{-/-}$) and 5 dpf (n = 23 WT, n = 11 *rasa1a*$^{-/-}$ and n = 11 *ephb4a*$^{-/-}$). **d**. Maximal intensity projection of the dorsal view of Tg(*kdrl:GFP);(gata1a:DsRed*) of the DLV of WT, *rasa1a*$^{-/-}$ and *ephb4a*$^{-/-}$ larvae with a choroidal malformation at 3 dpf. The white arrows indicate two perfused vessels on the anterior and/or 2 perfused vessels on the posterior segment of the DLV. Scale bars, 300 µm for (**c**) and 50 µm for (**d**).

https://doi.org/10.1038/s44161-025-00659-5

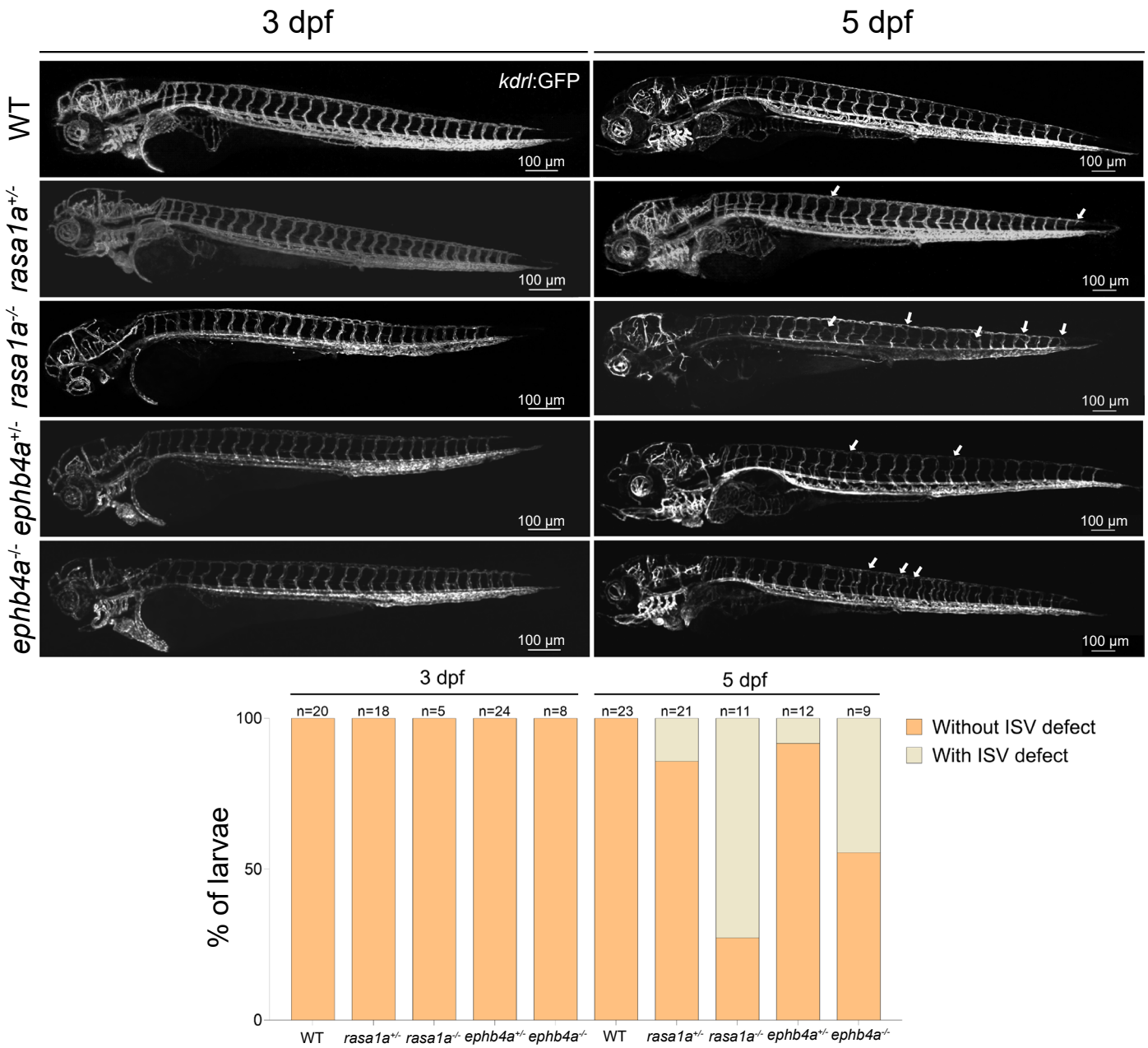

Extended Data Fig. 2 | Systemic vasculature in *rasa1a* and *ephb4a* mutants. Maximal intensity projection of a z-stack of WT, *rasa1a*$^{+/-}$, *rasa1a*$^{-/-}$, *ephb4a*$^{+/-}$ and *ephb4a*$^{-/-}$ Tg(*kdrl*:GFP) larvae at 3 dpf (n = 20 WT, n = 18 *rasa1a*$^{+/-}$ n = 5 *rasa1*$^{-/-}$, n = 24 *ephb4a*$^{+/-}$ and n = 8 *ephb4a*$^{-/-}$) or 5 dpf (n = 23 WT, n = 21 *rasa1a*$^{+/-}$ n = 11 *rasa1*$^{-/-}$, n = 12 *ephb4a*$^{+/-}$ and n = 9 *ephb4a*$^{-/-}$). White arrows indicate regions of ISV defects, such as duplication or lack of perfusion. Quantification of ISV malformations in WT, *rasa1a*$^{+/-}$, *rasa1a*$^{-/-}$, *ephb4a*$^{+/-}$ and *ephb4a*$^{-/-}$ larvae at 3 dpf and 5 dpf. Scale bars, 100 µm.

https://doi.org/10.1038/s44161-025-00659-5

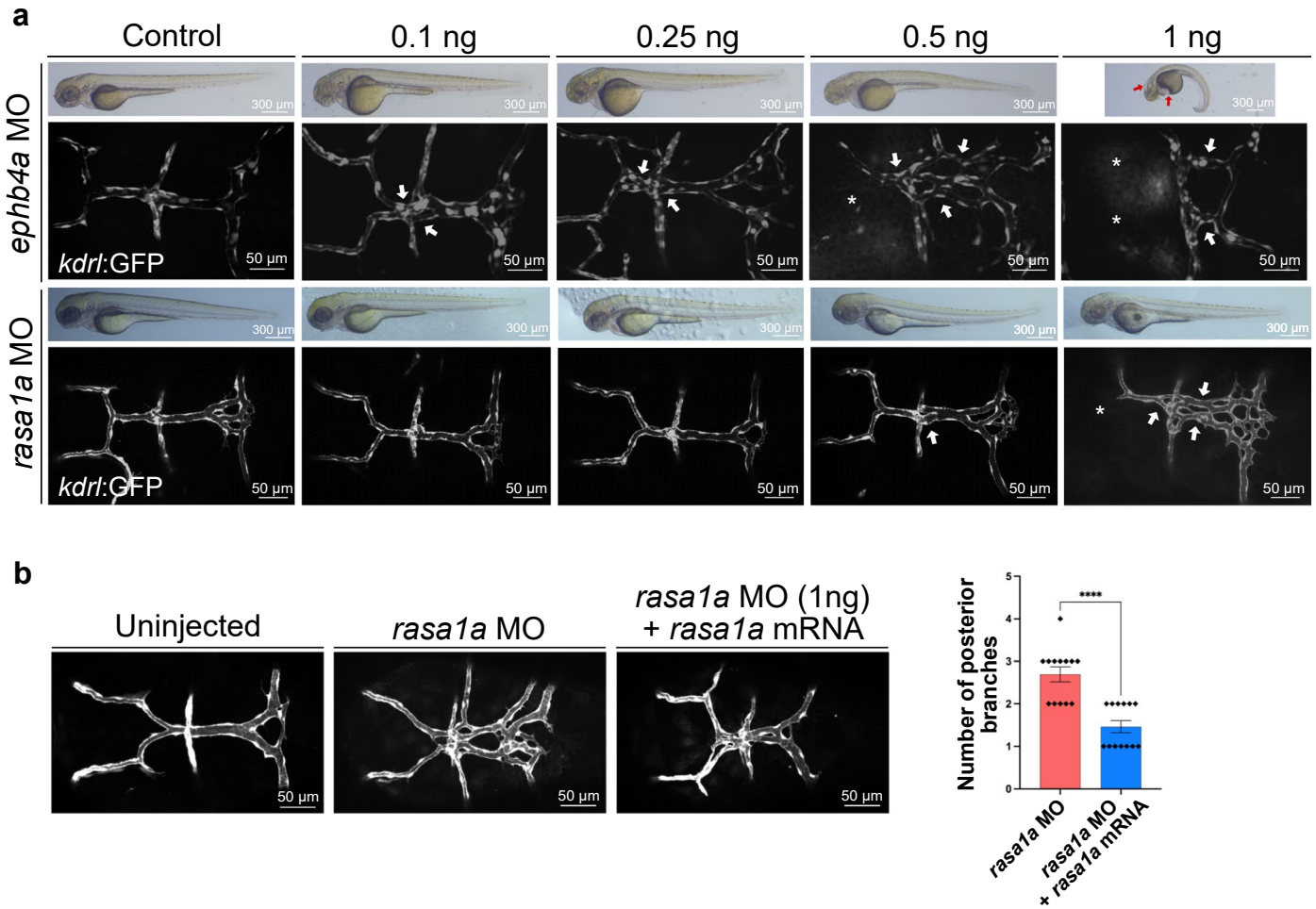

Extended Data Fig. 3 | Effect of *rasa1a* and *ephb4a* MO injection. a. Lateral views of larvae at 3 dpf and maximal intensity projection of *Tg(kdrl:GFP)* of DLV in WT larvae at 3 dpf injected with different doses of *ephb4a* and *rasa1a* morpholinos. Injection of *ephb4a* morpholino at 0.5 ng and *rasa1a* morpholino at 1 ng resulted in duplication or triplication of the DLV (white arrow) and absence of the mesencephalic veins (MsV) (asterisk). At higher concentrations of *ephb4a* morpholino, cardiac and cerebral edema (red arrow) were observed. **b.** Maximal intensity projection of *Tg(kdrl:GFP)* of DLV in WT larvae at 3 dpf injected with 1 ng of *rasa1a* morpholino or with 1 ng of *rasa1a* morpholino and *rasa1a* mRNA (100 ng, *rasa1a* CDS inserted in pminiTol2 backbone). Quantification of the number of dorsal vessels was performed (mean +/- SEM, non parametric t test, ****: $p < 0{,}0001$) **c.** Dorsal view of the brain vasculature network at 3 dpf of WT embryos injected with 1 ng of morpholino against *rasa1a*. Scale bars, 300 µm and 50 µm for (**a** and **b**) and 250 µm for (**c**).

https://doi.org/10.1038/s44161-025-00659-5

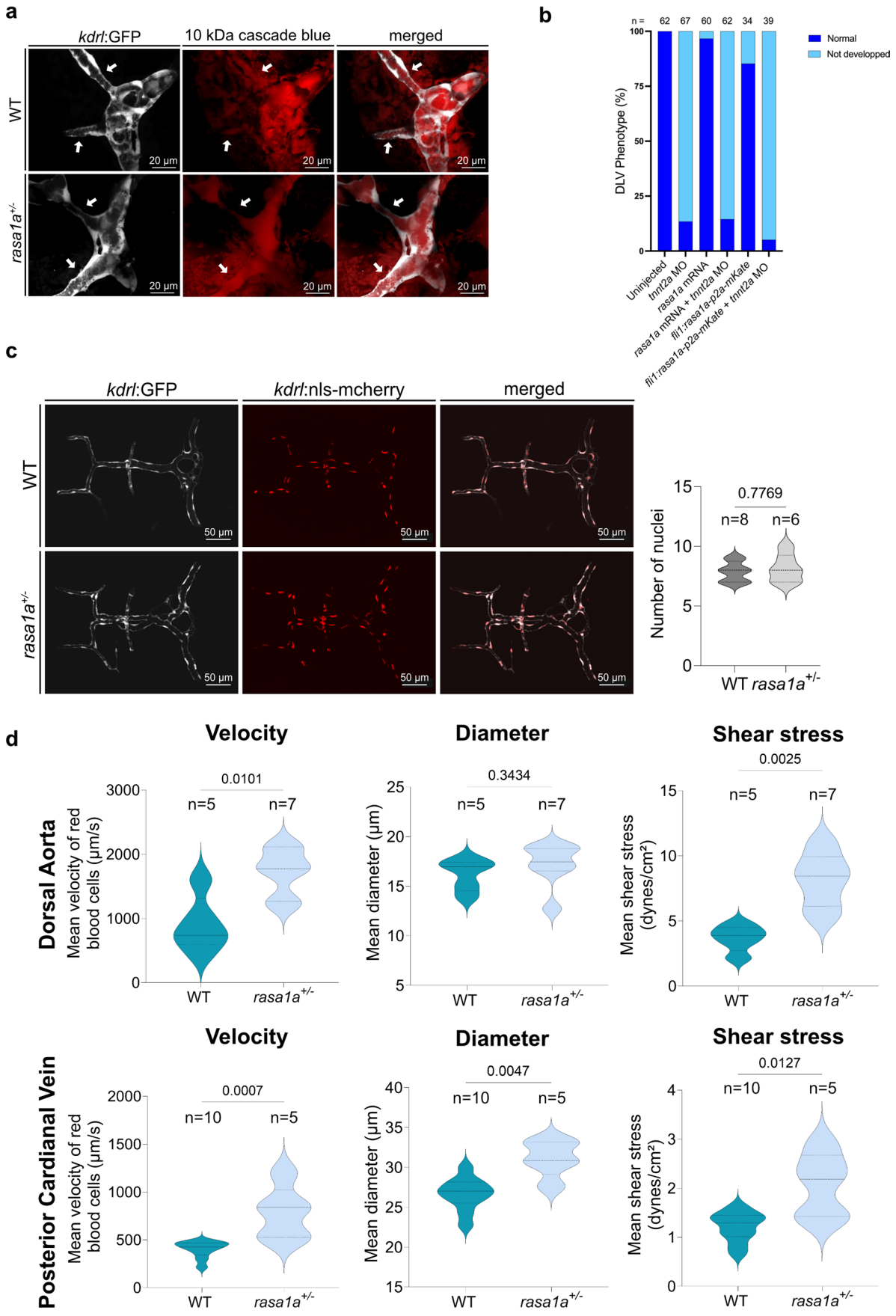

Extended Data Fig. 4 | See next page for caption.

https://doi.org/10.1038/s44161-025-00659-5

Extended Data Fig. 4 | Blood flow in the development of the DLV. a. Analysis of vessel perfusion by fluorescent tracer injection (10 kDa cascade blue) into the duct of Cuvier at 36 hpf. The preliminary vascular structure leading to the formation of the DLV was perfused at 36 hpf in WT and *rasa1a*$^{+/-}$ embryos. **b**. Quantification of DLV development after injection of tnnt2a MO (0.25 µg) with or without co-injection with rasa1a mRNA (100 ng, *rasa1a* CDS inserted in pminiTol2 backbone) or 15 pg of *pminiTol2_fli1:rasa1a-p2A-mKate* vector for specific expression in endothelial cells **c**. Maximum projection of the vascular network of the DLV in WT and *rasa1a*$^{+/-}$ *Tg(kdrl:nls-mCherry);(kdrl:GFP)* double transgenics. Quantification of the number of nuclei in the DLV (n = 8 WT, n = 6 *rasa1a*$^{+/-}$, Mann–Whitney U test). **d**. Quantification of DA and PCV blood flow parameters: velocity (DA: n = 5 WT, n = 7 *rasa1a*$^{+/-}$; PCV: n = 10 WT, n = 5 *rasa1a*$^{+/-}$), diameter (DA: n = 5 WT, n = 7 *rasa1a*$^{+/-}$; PCV: n = 10 WT, n = 5 *rasa1a*$^{+/-}$) and shear stress (DA: n = 5 WT, n = 7 *rasa1a*$^{+/-}$; PCV: n = 10 WT, n = 5 *rasa1a*$^{+/-}$) in WT and *rasa1a*$^{+/-}$ at 3 dpf (Mann-Whitney U test). Scale bars, 20 µm for (**a**) and 50 µm for (**c**).

nature portfolio

Corresponding author(s): Nicolas Baeyens

Last updated by author(s): 28/03/2025

Reporting Summary

Nature Portfolio wishes to improve the reproducibility of the work that we publish. This form provides structure for consistency and transparency in reporting. For further information on Nature Portfolio policies, see our Editorial Policies and the Editorial Policy Checklist.

Statistics

For all statistical analyses, confirm that the following items are present in the figure legend, table legend, main text, or Methods section.

n/a	Confirmed	
☐	☒	The exact sample size (*n*) for each experimental group/condition, given as a discrete number and unit of measurement
☐	☒	A statement on whether measurements were taken from distinct samples or whether the same sample was measured repeatedly
☐	☒	The statistical test(s) used AND whether they are one- or two-sided *Only common tests should be described solely by name; describe more complex techniques in the Methods section.*
☒	☐	A description of all covariates tested
☐	☒	A description of any assumptions or corrections, such as tests of normality and adjustment for multiple comparisons
☐	☒	A full description of the statistical parameters including central tendency (e.g. means) or other basic estimates (e.g. regression coefficient) AND variation (e.g. standard deviation) or associated estimates of uncertainty (e.g. confidence intervals)
☐	☒	For null hypothesis testing, the test statistic (e.g. *F*, *t*, *r*) with confidence intervals, effect sizes, degrees of freedom and *P* value noted *Give P values as exact values whenever suitable.*
☒	☐	For Bayesian analysis, information on the choice of priors and Markov chain Monte Carlo settings
☒	☐	For hierarchical and complex designs, identification of the appropriate level for tests and full reporting of outcomes
☒	☐	Estimates of effect sizes (e.g. Cohen's *d*, Pearson's *r*), indicating how they were calculated

Our web collection on statistics for biologists contains articles on many of the points above.

Software and code

Policy information about availability of computer code

Data collection	For each sample, the displacement of erythrocytes required an acquisition speed of 200 frames per second with a number of 3000 frames. This acquisition speed allows automated analysis of the velocities by tracking the erythrocytes individually, image by image, via the scientific imaging software Fiji and the image analysis module "TrackMate v7". This software allows both to obtain the plot of the instantaneous velocities of erythrocytes and calculate the average velocity of these by integrating the velocity peaks.
Data analysis	For the calculation of the fundamental frequency, the frequency profile (Figure 2) and blood parameters (Extended data Figure 2) , we used a spinning disk confocal microscope (X-Light V3, Crest optics) equipped with a fast camera (Prime BSI Scientific CMOS (sCMOS)) with an acquisition speed of 750 frames per second and a NiR Apo 40x/0,80 DIC N2 water immersion objective. The fundamental frequency of the red blood cells' velocity was programmatically assessed using MATLAB version R2021b. Velocity and time data generated by "TrackMate v7" were imported as vectors. The sampling frequency was calculated as the inverse of the average time step between each point of the time vector. Subsequently, a frequency vector was computed using the formula f = (0:n-1)(fs/n), following the Nyquist-Shannon sampling theorem. The discrete Fourier transform of the velocity vector was then computed using the FFT function. The findpeaks function was applied to the FFT spectrum to identify the peak corresponding to the fundamental frequency. Finally, the peak position was used to determine the value of the fundamental frequency. To demonstrate the generation of two independent streams, the tracks of red blood cells produced by "TrackMate" were sorted using a Python program (Jupyter Notebook version 6.4.5 running using conda 4.14.0 and Python 3). For each track, the initial and final positions of the red blood cells were identified with respect to the x and y axis. A central axis was then created to follow the direction of the DLV. Tracks were then sorted based on the position of their initial ad final points relative to the central axis. Tracks were then assigned different colors based on this sorting.

For manuscripts utilizing custom algorithms or software that are central to the research but not yet described in published literature, software must be made available to editors and reviewers. We strongly encourage code deposition in a community repository (e.g. GitHub). See the Nature Portfolio guidelines for submitting code & software for further information.

Data

Policy information about availability of data

All manuscripts must include a data availability statement. This statement should provide the following information, where applicable:

- Accession codes, unique identifiers, or web links for publicly available datasets
- A description of any restrictions on data availability
- For clinical datasets or third party data, please ensure that the statement adheres to our policy

Provide your data availability statement here.

Research involving human participants, their data, or biological material

Policy information about studies with human participants or human data. See also policy information about sex, gender (identity/presentation), and sexual orientation and race, ethnicity and racism.

Reporting on sex and gender	Sex of the two patients (male) was reported in the Figure 1A legend. Sex was not considered in the study design as they are only illustrative exemples of the malformations studied in the article.
Reporting on race, ethnicity, or other socially relevant groupings	No reporting on race, ethnicity or other socially relevant groupings were made in this study
Population characteristics	1 patient male 5 years old, 1 patient male neonate
Recruitment	retrospective analysis of our pediatric patient database
Ethics oversight	Ethics committee of Erasme hospital, HUB, Brussels

Note that full information on the approval of the study protocol must also be provided in the manuscript.

Field-specific reporting

Please select the one below that is the best fit for your research. If you are not sure, read the appropriate sections before making your selection.

☒ Life sciences ☐ Behavioural & social sciences ☐ Ecological, evolutionary & environmental sciences

For a reference copy of the document with all sections, see nature.com/documents/nr-reporting-summary-flat.pdf

Life sciences study design

All studies must disclose on these points even when the disclosure is negative.

Sample size	No sample size calculations were performed. Minimum sample size was three independent samples/repeated experiments, corresponding to standards in the field
Data exclusions	No data were excluded
Replication	Every experiment/observation has been repeated independently a minimum of three times.
Randomization	Randomization was the norm for every experiment, when possible. Embryos were randomly allocated a drug in figures 7 and 8. Genotype distribution could not be controlled prior the experiment, genotype validation was always performed once the experiment completed by clip fin, ensuring randomization and blinding.
Blinding	Blinding was performed to characterize the distribution of the phenotype of both mutants and another investigator validated the observations. Blinding was not performed on other experiments as it was conducted by a single experimentator

Reporting for specific materials, systems and methods

We require information from authors about some types of materials, experimental systems and methods used in many studies. Here, indicate whether each material, system or method listed is relevant to your study. If you are not sure if a list item applies to your research, read the appropriate section before selecting a response.

Materials & experimental systems

n/a	Involved in the study
☐	☒ Antibodies
☐	☒ Eukaryotic cell lines
☒	☐ Palaeontology and archaeology
☐	☒ Animals and other organisms
☐	☒ Clinical data
☒	☐ Dual use research of concern
☒	☐ Plants

Methods

n/a	Involved in the study
☒	☐ ChIP-seq
☒	☐ Flow cytometry
☒	☐ MRI-based neuroimaging

Antibodies

Antibodies used	beta-actin (Sigma #A5441); peacm1 (R&D #AF3628); phospho AKT Ser473 (Cell Signaling #4060); phospho ERK1/2 Thr202/Tyr204 (Proteintech #28733-1-AP); rasa1 B4F8 (Invitrogen # MA4-001); Anti-mouse IgG (H+L) DyLight 680 conjuguate (Cell Signalling #5470); Anti-rabbit IgG (H+L) DyLight 800 4x PEG conjuguate (Cell Signaling #5151); Donkey anti-goat IgG (H+L) Highly cross-adsorbed secondary antibody AlexaFluor Plus 555 (Thermo Fisher #A32816)
Validation	Rasa1 ab validated by knock-down. Actin antibody validated on cell/tissue extracts. PECAM1 ab validated biologically, Phospho Akt validated biologically, Phospho ERK validated by KD/KO

Eukaryotic cell lines

Policy information about cell lines and Sex and Gender in Research

Cell line source(s)	HUVECs were purchased from Lonza
Authentication	Tested positive for CD31 and CD105
Mycoplasma contamination	Tested free of mycoplasma by manufacturer
Commonly misidentified lines (See ICLAC register)	HUVECs are not commonly misidentified cells

Animals and other research organisms

Policy information about studies involving animals; ARRIVE guidelines recommended for reporting animal research, and Sex and Gender in Research

Laboratory animals	Zebrafish (animals used in experimental procedures were from 36 to 96 hours post fertilization)
Wild animals	No wild animals were used in this study
Reporting on sex	Sex of the zebrafish larva was not reported in this study
Field-collected samples	No field-collected samples were used in this study
Ethics oversight	Local ethics committee CEBEA: CEBEA 07-GOS-IBMM

Note that full information on the approval of the study protocol must also be provided in the manuscript.

Clinical data

Policy information about clinical studies

All manuscripts should comply with the ICMJE guidelines for publication of clinical research and a completed CONSORT checklist must be included with all submissions.

Clinical trial registration	Protocol number P2022/256 "Prise en charge des anomalies cérébrales vasculaires chez l'enfant à l'hopital Erasme"
Study protocol	Retrospective study on VGAM patients (clinical images)
Data collection	From 01/01/2010 to 01/05/2022
Outcomes	N/A

Plants

Seed stocks	No seed stocks were used in this study
Novel plant genotypes	No plants were used in this study
Authentication	N/A